Digital Control of a Wireless Power Transfer System for Electrical Vehicles

C. Riekerk

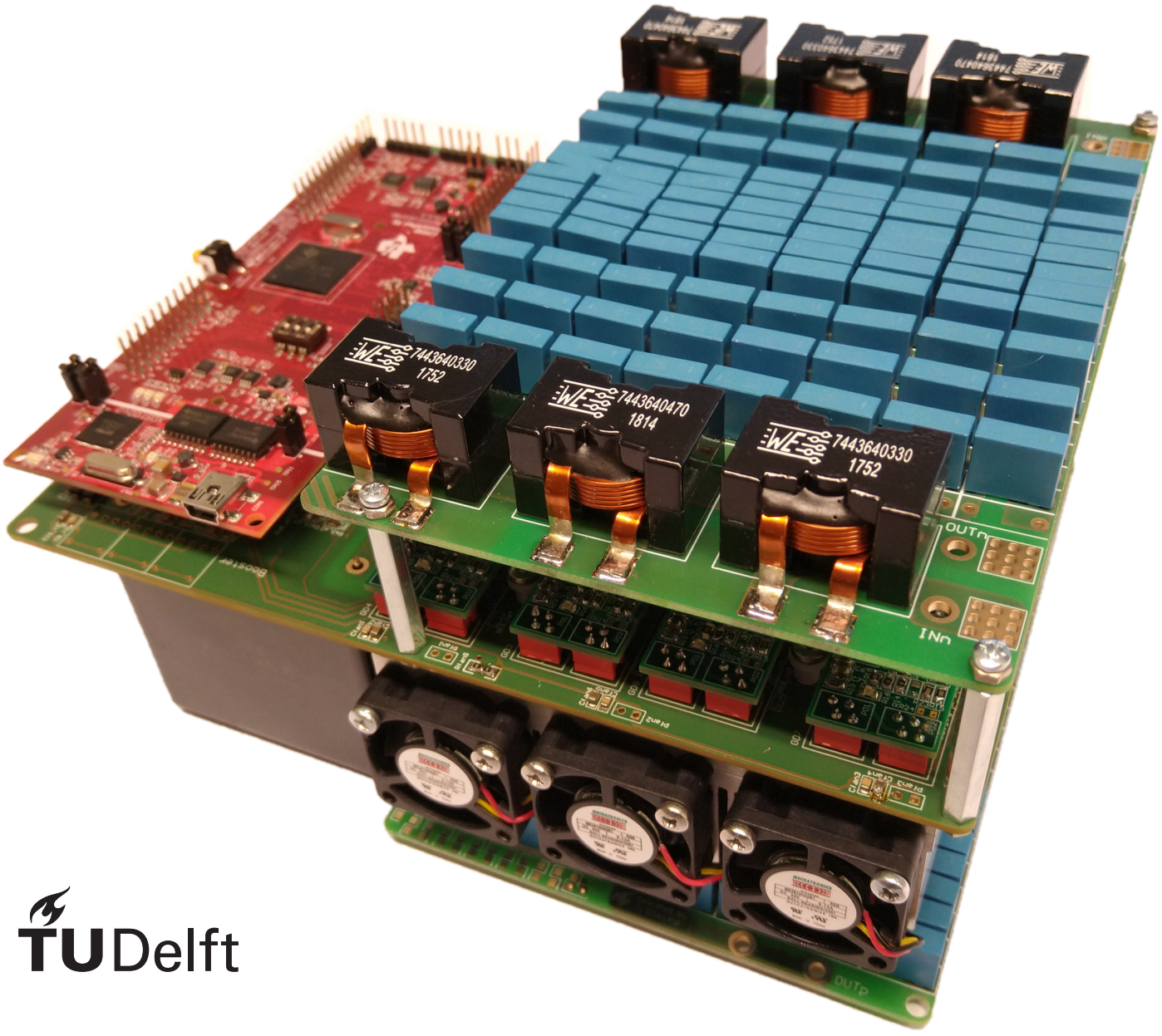

TU Delft

Digital Control of a Wireless Power Transfer System for Electrical Vehicles

by

C. Riekerk

to obtain the degree of Master of Science
at the Delft University of Technology,
to be defended publicly on Monday June 29, 2020 at 13:30.

Student number:	4467450	
Project duration:	November 11, 2019 – June 29, 2020	
Daily supervisor:	F. Grazian MSc. ,	TU Delft
Thesis committee:	Prof. dr. ir. P. Bauer ,	TU Delft, supervisor
	Dr. T. B. Soeiro ,	TU Delft, daily supervisor
	Dr. ir. J. L. Rueda Torres ,	TU Delft

An electronic version of this thesis is available at `http://repository.tudelft.nl/`.

TU Delft

Abstract

Wireless power transfer (WPT) is becoming a popular choice for charging of batteries in various applications. Particularly, the increase in popularity of electrical vehicles (EVs) and the pursuit of user convenience for charging the batteries makes WPT an attractive solution. The usage of WPT in e-transportation is not straightforward because the current standardization limits the allowed frequency operating range and magnitude of the irradiated magnetic field. Additionally, a fast control loop with high current or voltage sensing bandwidth is necessary to guarantee soft-switching of the inverter's semiconductors which are commonly employed as part of an equivalent DC-DC resonant converter. The resonant circuit typically comprises of a H-bridge inverter, two passive compensation network one at each side of the air-gapped transformer formed by a transmitter and a receiver coil, and a diode-bridge rectifier. The control of the resonant converter can be cumbersome particularly in case of dynamic charging condition because of the natural change in equivalent load and coil misalignment conditions which cause the magnetic coupling to change.

The main goals of this thesis are: to understand the challenges involved with the control of WPT for EVs; to propose and implement a digital control strategy for WPTs which not only maintain soft-switching but also realize other functionalities such as soft start-up, soft shut-down and over-current protection.

With respect to power efficiency, it is important to operate the inverter with a frequency which makes the resonant converter to function in the inductive region enabling soft-switching turn-on of the implemented active semiconductors, such as MOSFETs. For that reason the inverter is typically operated at a frequency slightly above the resonance, however this must avoid the effect of bifurcation. Studies in the literature have found that the efficiency of the system is typically the highest at maximal magnetic coupling between the coils and when the resonant circuit impedance match the so-called optimal load resistance. Furthermore, the current available standards have set narrow requirements on the frequency range, minimum power efficiency and restriction of irradiated magnetic field for both, safety of living beings and electromagnetic compatibility. All these requirements makes the control implementation of WPT very challenging, especially for high power applications.

In this work, the closed-loop control is successfully integrated into a TI microcontroller where the soft-switching mechanism is derived with a selective band zero crossing detection circuit of the inverter AC current. The current band is used to tune the instant where the semiconductor bridge turns from ON to OFF state because there is a minimal current that need to be impressed into the inverter to reach the desired soft-switching by compensating the accumulated charges across the parasitic MOSFET capacitances. This is also important to compensate the signal processing delays of the closed-loop control. This functional block is implemented externally to the TI digital controller with the existing high bandwidth current sensing and commercial analog logic ICs. Moreover, an over-current protection is incorporated into the zero crossing block, achieving a reaction time of 66ns. Finally, several strategies are proposed and tested for the soft start-up and a concept is made for the soft shut-down of a WPT experimental setup available in the laboratory.

Preface

This thesis about the "Digital Control of a Wireless Power Transfer System for Electrical Vehicles" has been written to fulfill the final requirement to obtain the "Master of Science" degree at the Delft University of technology. The work has been performed at the electrical sustainable energy department, in the DC systems. energy conversion and storage group.

I could not have finished this thesis without all the support I have gotten during this whole process. So, I want to start thanking these people. First, I want to thank my daily supervisor Francesca Grazian. You have taught me a lot of things about wireless power transfer, have helped me out a lot in the lab and have provided excellent feedback on my thesis. Words can hardly describe how grateful I am.

Next, I want to show my gratitude to Thiago Batista Soeiro who is also my daily supervisor. Your feedback on my thesis was invaluable. Furthermore, you always encouraged me throughout the whole process and provided excellent advice and insight.

Afterward, I want to thank Pavol Bauer for being my official supervisor and José Rueda Torres for being part of my thesis committee and taking some time to read my thesis.

I also want to express my gratitude to my friends for offering me some time to relax and clear my mind. Lastly, I want to thank my parents for supporting throughout my whole journey. The support you have given me has always allowed me to push myself even further.

C. Riekerk
Delft, June 2020

Contents

1 Introduction

In the last decades, wireless power transfer (WPT) has become more commonly used in different battery charging applications mostly in the form of inductive power transfer (IPT). For example, it has been implemented in medical implants [1], smartphones [2] and robotics [3]. The basic principle of WPT is that a primary coil generates a magnetic field that induces a current in a secondary coil, in which the working phenomena is modelled by Ampère's and Faraday's law [4]. Because the WPT coils are typically separated with large air gaps a loose magnetic coupling between them is common due to relatively large stray fields. Hence, compensation capacitors are added to solve the issue regarding the loose coupling [5]. The compensation capacitors counteract the reactive current created by the high leakage inductance and magnetizing current. This will significantly increase the efficiency of the WPT system. With the rise of popularity of EVs, it has become interesting to implement the battery charging with WPT systems mostly because of user's convenience. The WPT replaces the used cable in contact charging solutions which is vulnerable to weather effects and vandalism [6].

The implementation of WPT for EV charging is regulated by international standards. For example, the operating frequency range of the fundamental transferred magnetic field must be within 81.38-90 kHz [7]. The consequence of this is that the inverter at the primary side must operate within the same frequency range. By controlling the frequency and duty cycle of the primary inverter, it is possible to regulate the power transmitted to the secondary side. Additionally, if the secondary DC voltage or current do not match the required value from the battery, it is possible to use a DC/DC converter to adjust the required operation. The typical structure of a WPT charging system is shown in Figure 1.1.

A relative high frequency is used for the inverter in which it needs to provide soft-switching of the semiconductors while ensuring: lower energy losses and reduced electromagnetic interference or EMI [8]. This means that a fast control loop strategy is necessary. The next challenge is that the position of the car has a great impact on the coupling between the coils because a misalignment condition could occur. If the coils are well aligned, it would result in a higher coupling between the coils. However, the position of the car is not always the same. This means that the coupling between the coils could differ every time the car is parked. Moreover, the equivalent load varies over time because the battery's state of charge changes during the charging process. These factors influence the optimum operating condition that maximizes the efficiency of the primary and secondary coils. This means that the operating point must be adjusted to ensure a high efficiency of the WPT system.

The research objectives of the project are:

- To understand the challenges involved with the control of WPT for EVs.
- To program the digital control and integrate it with a fast analog current sensing and logic circuit to ensure the semiconductors operation with soft-switching in the allowed narrow frequency range.
- To implement other functionalities such as soft start-up, soft shut-down and over-current protection.

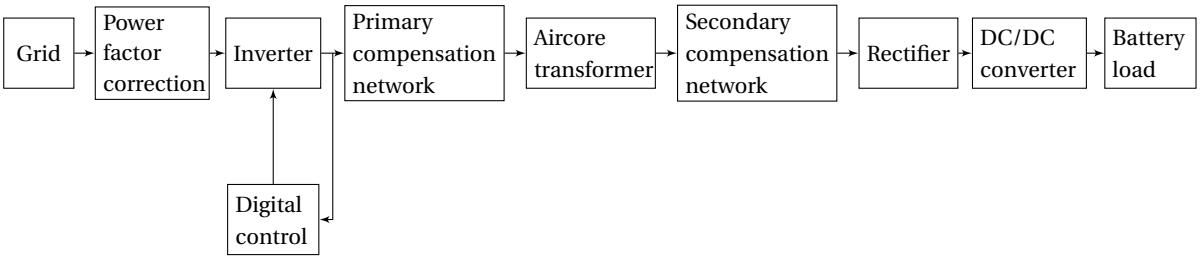

Figure 1.1: Block diagram of a general WPT system.

The methodology of this study is composed of several parts. First, a literature research is performed related to the characteristics of WPT systems and their control strategies. Then, an open-loop controller is designed and tested with the goal to verify the functionality and the suitability for the application of the commercial texas instruments (TI) F28379D Launchpad. Afterward, a closed-loop controller is designed and programmed in this digital microcontroller. This should be integrated with the already existing analog zero crossing detection (ZCD) circuit implemented in a existing WPT prototype. Lastly, the extra proposed features for: soft start-up, soft shut-down and over-current protection are incorporated and tested.

The thesis is structured in the following way: Chapter 1 comprises the introduction containing: the background information, possible challenges, research objectives, methodology and thesis outline. Chapter 2 is the literature research. It includes the theory about the power electronics used in a WPT system, compensation networks, coil topologies, standards and different control strategies. Chapter 3 deals with the digital control implementation. It will show how the open-loop control has been programmed, the design of the analog ZCD circuit, the integration between the ZCD circuit and the digital closed-loop controller, the implementation of the soft start-up with a comparison between two popular passive resonant compensation circuits, the LCC and S-S compensation, and a concept on the soft shut-down. Chapter 4 is the conclusion which describes the technical finds and future work.

2

Literature Research

2.1. Power Electronics

Power electronic circuits are an essential part in the WPT system. They allow for power conversion between AC and DC quantities. This chapter gives a brief explanation about the (PFC) power factor correction converter and the isolated DC/DC resonant converter.

2.1.1. Power Factor Correction Converter

The grid-connected power electronic circuit comprises a power factor corrector (PFC) converter with a possible circuit implementation as shown in Figure 2.1. The PFC operates in such a way that the system display a resistive-like load behaviour or that the AC current waveform drained from the grid is in phase and with the same shape with the voltage of the grid as shown in Figure 2.2. As a consequence, this will increase the power factor and reduce the current total harmonic distortion (THD). It is especially important to reduce current harmonic components to improve the power quality in the grid and to reduce electromagnetic interference with other devices connected to the same grid [9].

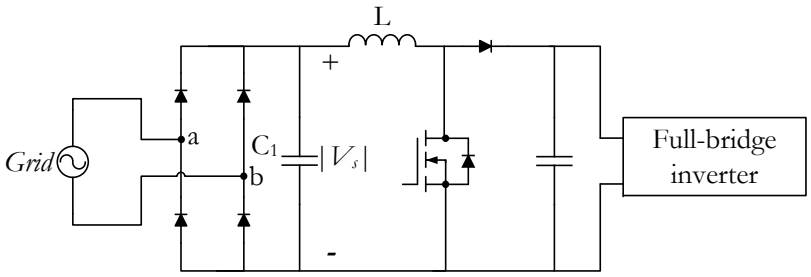

Figure 2.1: PFC boost converter.

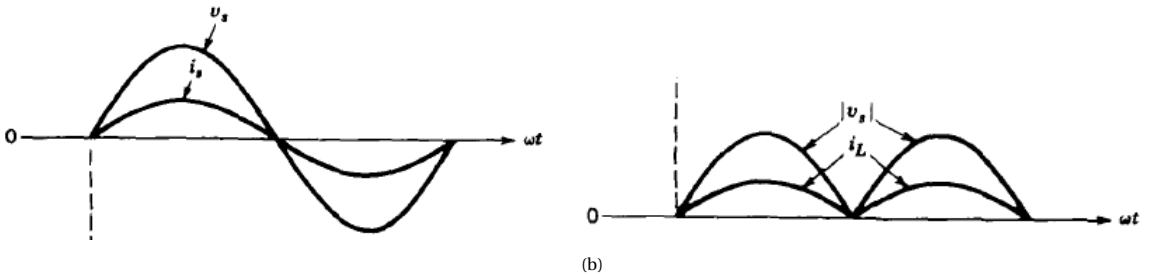

(a) (b)

Figure 2.2: The voltage and current: (a) at the grid and (b) after the rectifier [8].

In Figure 2.1, the PFC converter varies the switching state of the MOSFET to either store energy or discharge it to/from the inductor. Note that the circuit connected at the output of the diode-bridge rectifier is a conventional DC/DC boost converter. Because of the alternate switching between the charging and discharging states, the output current of the grid will look like the one shown in Figure 2.3. Therefore, further AC passive filtering is commonly employed for high-frequency current harmonic mitigation and grid-code compliance. Furthermore, it is important that the DC/DC converter controls the output voltage to be delivered to the inverter as a DC quantity with low voltage ripples. Finally, the PFC ensures that the grid voltage is in phase with the AC current [10].

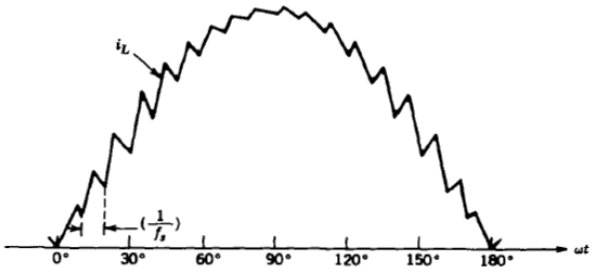

Figure 2.3: The inductor current of the PFC converter [8].

2.1.2. Half-Bridge Inverter

The half-bridge inverter is shown in Figure 2.4. The voltage over the capacitors C_1 and C_2 is equal to half of the source voltage. Both switches S_1 and S_2 can not be on at the same time as this would create a short-circuit of the DC input voltage. Consequently the switching of S_1 and S_2 will have an opposite switching state to each other. When S_1 is closed and S_2 is open, the inverter output voltage will be equal to $\frac{V_s}{2}$, and for the opposite case it will be $-\frac{V_s}{2}$. In this way, the output of the inverter would result in a square wave that varies between $\frac{V_s}{2}$ and $-\frac{V_s}{2}$.

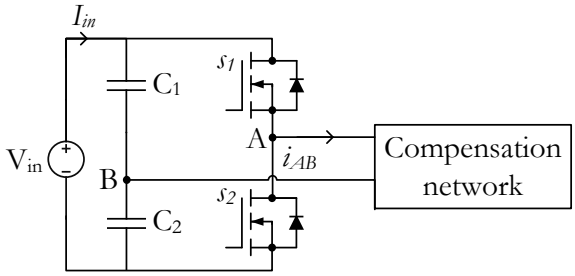

Figure 2.4: Half-bridge inverter.

The voltage and current stress on the switches are [8]:

$$V_Q = V_S \tag{2.1}$$

$$I_Q = I_{out,peak} \tag{2.2}$$

2.1.3. H-Bridge Inverter

The H-bridge inverter is shown in Figure 2.5. To create a square wave voltage at the output, implementing the so-called bipolar PWM modulation, the inverter will alternate between either having S_1 and S_4 closed while S_2 and S_3 open or having S_2 and S_3 closed while S_1 and S_4 are open. The square wave varies between V_s and $-V_s$.

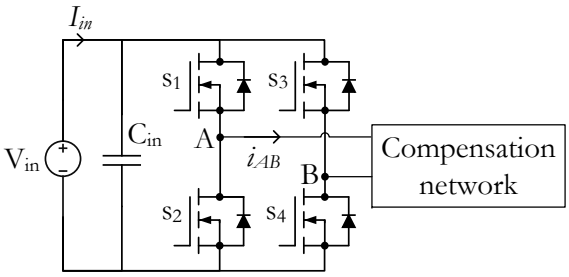

Figure 2.5: H-bridge inverter.

The voltage stress across the switches are the same as for the half-bridge inverter [8]. In the case of high power applications, it is preferred to use a H-bridge configuration instead of a half-bridge one because of less current stress on the switches for the same power level.

2.1.4. Full-Bridge Diode Rectifier

At the secondary-side of the WPT charging system, a full-bridge diode rectifier as shown in Figure 2.6 is used. It is used to convert the AC voltage and current from the compensation network to a DC voltage and current to charge the DC battery.

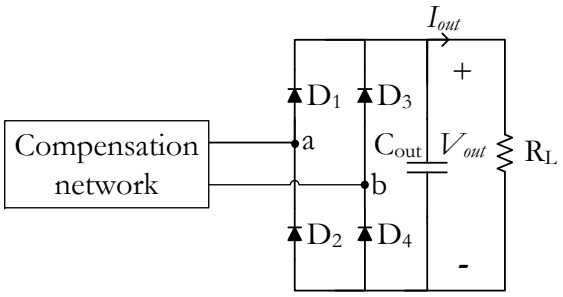

Figure 2.6: Full-bridge rectifier.

The diodes D_1 and D_4 will conduct for the positive half cycle of the secondary side voltage. If the secondary side voltage is in a negative half cycle then D_2 and D_3 will conduct. Capacitor C_{out} is used as a smoothing voltage/current filter [8].

2.1.5. Series Resonant Converter

The series resonance converter is shown in Figure 2.7. It consists of a H-bridge inverter, an inductor and capacitor connected in series, a transformer and a rectifier. It should be noted that the total leakage inductance of the transformer is referred to the primary circuit, and it is represented by the equivalent inductance L_1.

It is important to study the behaviour of this converter as it has a similar operation as a general WPT system. The main difference is that the transformer is not loosely coupled and one can assume that the coupling factor stays at a constant value. The converter has three operating modes based on the switching frequency of the inverter and the resonance frequency of L_1 and C_1 [8]. The resonance frequency is given by:

$$f_r = \frac{1}{2\pi\sqrt{L_1 C_1}} \tag{2.3}$$

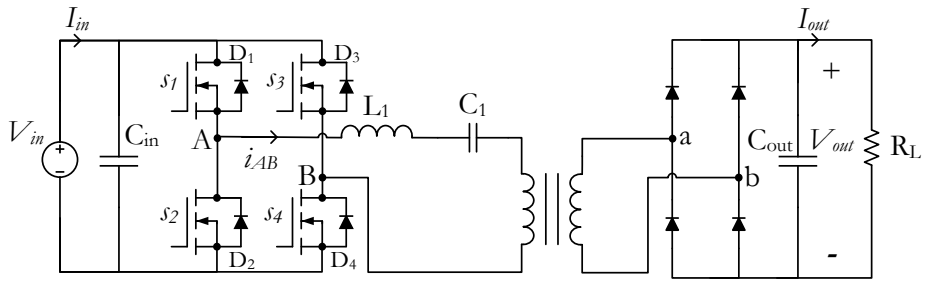

Figure 2.7: Series resonant converter.

Figure 2.8 shows the operation for f_s<0.5f_r. The switches S_1 and S_4 conduct for the first half period of the resonance frequency and, in the second half period, D_1 and D_4 will conduct because the inductor and capacitor are fully charged and the switches S_2 and S_3 are not yet ON. Afterward, the current becomes discontinuous. This discontinuous part is equal to half of the switching period minus the resonance period, because the resonance period ends when S_1, S_4, D_1, and D_4 conduct [8]. In the second half of the switching period a similar operation will happen, but then with S_2, S_3, D_2, and D_3. Furthermore, it can be observed from Figure 2.8 that the switches turn ON and OFF at zero current, the known zero current switching (ZCS). However, zero voltage switching (ZVS) is preferred over ZCS as it will reduce the turn-ON switching losses caused by the equivalent drain-source capacitance of the MOSFETs [11].

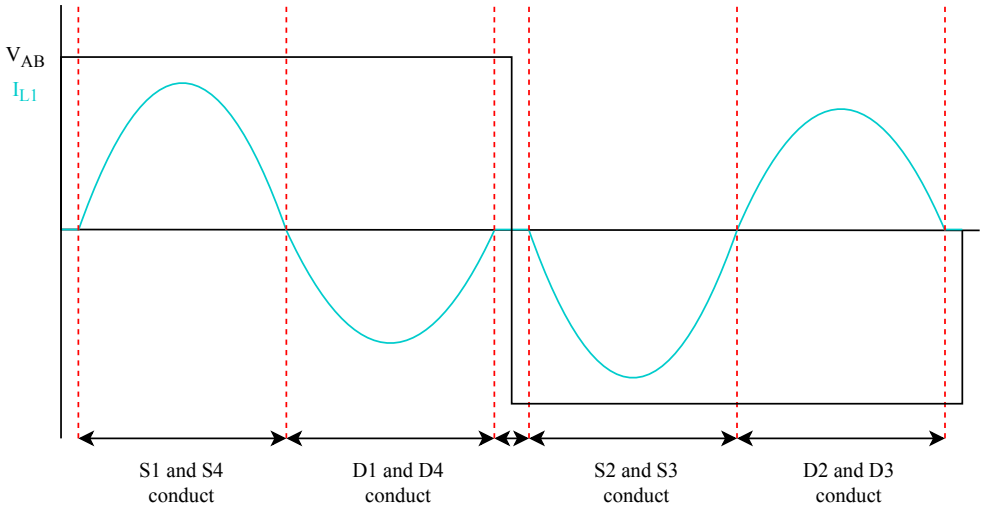

Figure 2.8: Output voltage of the inverter and inductor current for f_s<0.5f_r.

The waveforms for 0.5f_r<f_s<f_r are shown in Figure 2.9. From the figure, it can be seen that the voltage lags the current which shows a capacitive-like behavior. The current in the inductor reverses which allows D_2 and D_3 to conduct. It can be observed that the MOSFET S_1 and S_4 start conducting before the current has returned to zero which means that there will be a hard-switching turn-ON, but there is zero voltage turn-OFF which is guaranteed because the anti-parallel diode conducts the current before the MOSFET turns OFF [8].

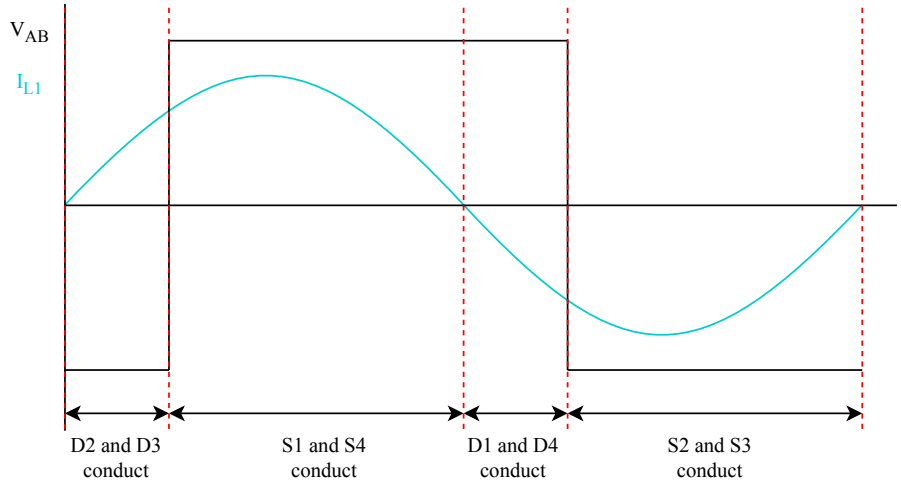

Figure 2.9: Output voltage of the inverter and inductor current for $0.5f_r<f_s<f_r$.

The main waveforms of the last operating mode are shown in Figure 2.10. The voltage leads the current which means that it shows an inductive-like behavior. This event leads to zero voltage turn-ON, because D_1 and D_4 conduct before S_1 and S_4 which leads to zero voltage turn-ON. The same happens for S_2 and S_3, but the MOSFET is forced to turn OFF at finite current. This introduces a hard-switching turn-OFF. However, by placing additional capacitors parallel to the MOSFET (a lossless snubber) can reduce turn-OFF losses, but to safeguard the ZVS turn-ON the switched current must be able to fully charge and discharge this capacitor.

The operating condition $f_s>f_r$ is desirable for the WPT charging system because the ZVS turn-ON. Additionally, it is important to tune the operation such that the switching frequency should only be slightly above the resonance frequency to maximize the power factor and the amount of power transferred, which is explained in more detail in chapter 2.2.4.

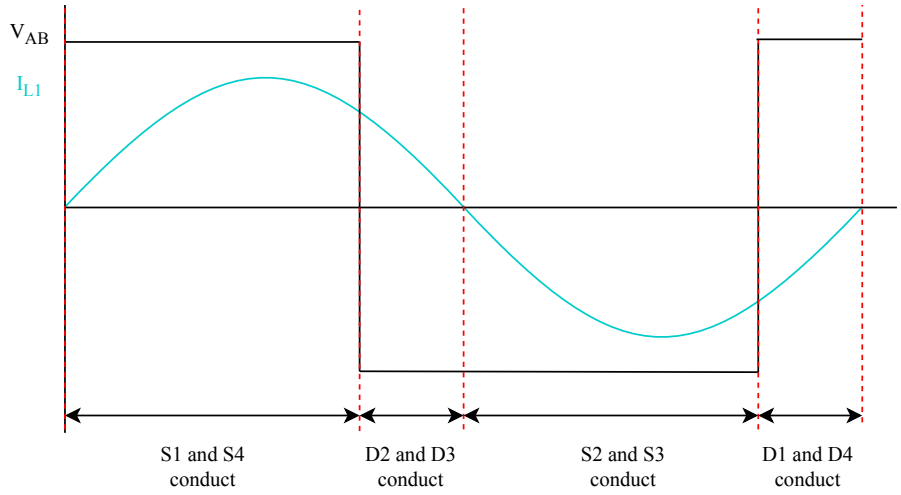

Figure 2.10: Output voltage of the inverter and inductor current for $f_s>f_r$.

2.2. Compensation Networks

Galvanic isolation is inevitable in WPT systems. In other applications, it is usually performed by a power factor correction rectifier and a DC-DC converter. In this case, the galvanic isolation is intrinsically caused by the large air gap between the primary and secondary coils which causes high leakage inductance and magnetizing current at the primary and secondary coils. It is then required that the input source has a high VA rating to transfer power to the load. This results in high reactive current which reduces the overall system efficiency. Compensation networks are used to counteract the reactive current by compensating the leakage inductance. A brief introduction to the basic compensation networks and the double-sided LCC compensation are given in this chapter. Furthermore an analysis is done on the effects of bifurcation, changes in the

coupling factor and changes of the load for a series-series compensation network.

2.2.1. Basic compensation network topologies

There are four basic network topologies which are implemented by placing capacitors either in series or parallel to the coils [4], [12].

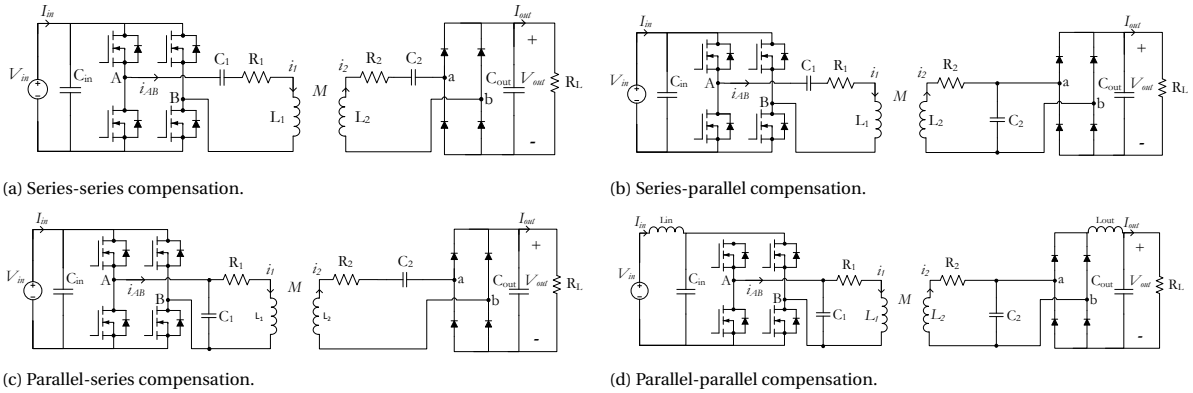

(a) Series-series compensation.

(b) Series-parallel compensation.

(c) Parallel-series compensation.

(d) Parallel-parallel compensation.

Figure 2.11: Basic compensation networks.

The value of the capacitor C_2 for all networks is given by:

$$C_2 = \frac{1}{\omega_0^2 L_2} \tag{2.4}$$

The mutual inductance is given by:

$$M = k\sqrt{L_1 L_2} \tag{2.5}$$

Table 2.1: Values of C_1 for the four basic compensation networks [12]

Compensation network	C_2
Series-series	$\frac{L_2 C_2}{L_1}$
Series-parallel	$\frac{L_2^2 C_2}{L_1 L_2 - M}$
Parallel-series	$\frac{L_1 L_2^2 C_2^2 R_3^2}{M^4 + L_1 L_2 R_3}$
Parallel-parallel	$\frac{L_2^2 C_2 (L_1 L_2 - M^2)}{(L_1 L_2 - M^2)^2 + M^4 R_3^2 L_2 C_2}$

From all four basic compensation networks only in the series-series topology the natural resonance is independent of the load and the coupling coefficient as shown in Table 2.1. This is important to consider for applications where these parameters changes which can happen if the load is a battery and if the coils are susceptible to misalignment.

2.2.2. Double-sided LCC compensation network

A more advanced compensation network would be a double-sided LCC network as shown in Figure 2.12. An advantage of this method is that the primary coil's current is less sensitive to load change [13], which is particularly advantageous in case of multiple secondary coils.

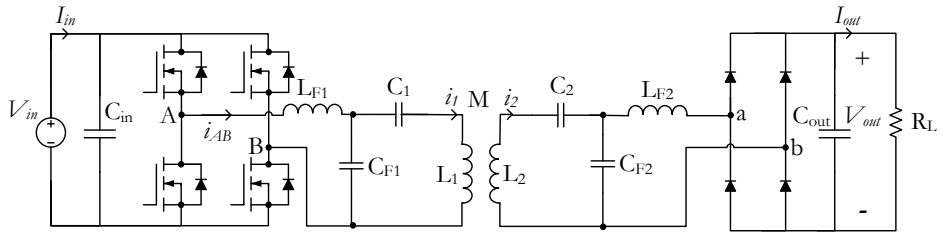

Figure 2.12: Double-sided LCC compensation network.

The transferred power of the compensation network is given by [13]:

$$P = \frac{MV_{AB}V_{out}}{\omega_0 L_{F1} L_{F2}} \tag{2.6}$$

To allow the use of ZVS turn-ON, it is necessary to have sufficient turn-OFF current to discharge C_{DS} within the dead time [11].

$$I_{off} > \frac{2V_{AB}C_{DS}}{t_{dead}} \tag{2.7}$$

$$C_{DS} = C_{OSS} - C_{RSS} \tag{2.8}$$

Then, it is possible to tune C_2 to achieve an acceptable turn-off current.

2.2.3. Bifurcation phenomenon

The bifurcation phenomenon also known as pole-splitting results in multiple frequencies where the phase angle of the input impedance is equal to zero and, among those frequencies, one is the chosen resonance frequency [12], [14]. The input impedance for a series-series compensation network is given by [15]:

$$Z_{in} = R_1 + j\omega L_1 + \frac{1}{j\omega C_1} + Z_r \tag{2.9}$$

Where R_1 is the series resistance of the primary coil, L_1 is the inductance of the primary coil, and C_1 is the capacitance of the primary compensation capacitor. The reflected impedance Z_r is given by (2.11).

$$Z_r = \frac{\omega^2 k^2 L_1 L_2}{R_L + R_2 + j\omega L_2 + \frac{1}{j\omega C_2}} \tag{2.10}$$

Substituting (2.10) into (2.9) results in:

$$Z_{in} = \underbrace{R_1 + \frac{\omega^4 C_2^2 k^2 L_1 L_2 (R_L + R_2)}{(\omega C_2)^2 (R_L + R_2)^2 + (\omega L_2 - 1)^2}}_{\text{Real Part}} + \underbrace{j\left(\omega L_1 - \frac{1}{\omega C_1} - \frac{\omega^3 C_2 k^2 L_1 L_2 (\omega^2 L_2 C_2 - 1)}{(\omega C_2)^2 (R_L + R_2)^2 + (\omega L_2 - 1)^2}\right)}_{\text{Imaginary Part}} \tag{2.11}$$

Equivalently, it can be said that the bifurcation occurs when the imaginary part of Z_{in} in (2.11) is equal to zero for multiple frequencies and not only for the chosen resonant frequency. The influence of the phenomenon is shown in Figure 2.13 by plotting the phase angle of Z_{in} for different frequencies. The values from Table 2.2 are used.

Table 2.2: The values used to simulate the bifurcation phenomenon.

Parameter	Value [unit]
L_1	70.28 [μH]
L_2	48.87 [μH]
C_1	35 [nF]
C_2	50 [nF]
R_1	0.09 [Ω]
R_2	0.12 [Ω]

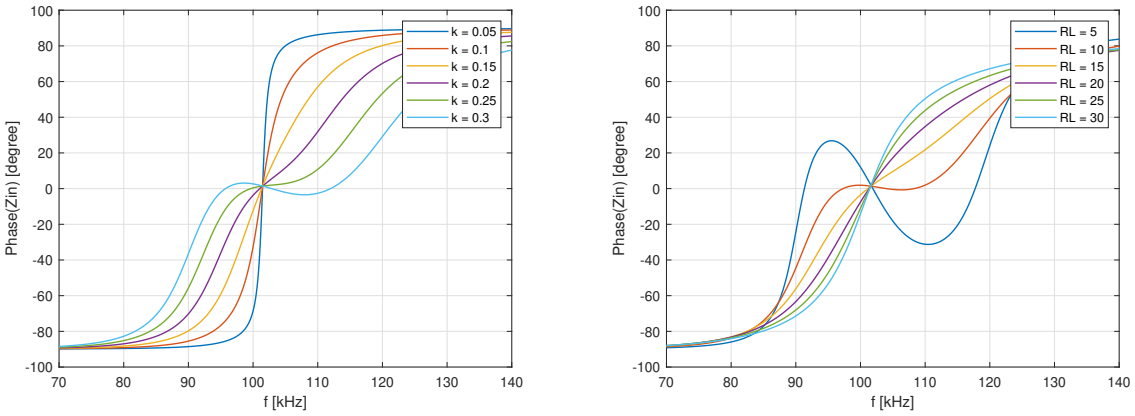

(a) Bifurcation for different k with R_{load} = 10 Ω.

(b) Bifurcation for different loads with k = 0.28.

Figure 2.13: The bifurcation phenomena for a series-series compensation network.

From Figure 2.13, it can be concluded that if the coupling factor k is increased or the load resistance is decreased, it will be more likely that bifurcation would occur. In WPT for EV charging, the coupling factor depends on the airgap between the two coils and the load resistance changes depending on the state of charge (SOC) of the battery, so it is important to prevent that bifurcation would occur for the nominal ranges of those variables. Furthermore, to achieve ZVS turn-ON of the inverter, it is needed that the voltage leads the current to get an inductive behaviour [13]. Normally, this would be accomplished by setting the switching frequency of the inverter just above the resonance frequency of the compensation network. However, if bifurcation would arise it could be that the system operates in the capacitive region in the case where the switching frequency of the inverter is found just above the resonance frequency.

2.2.4. Analysis Series-Series compensation circuit

The equivalent model in Figure 2.14 is used to analyse the series-series compensation network [12].

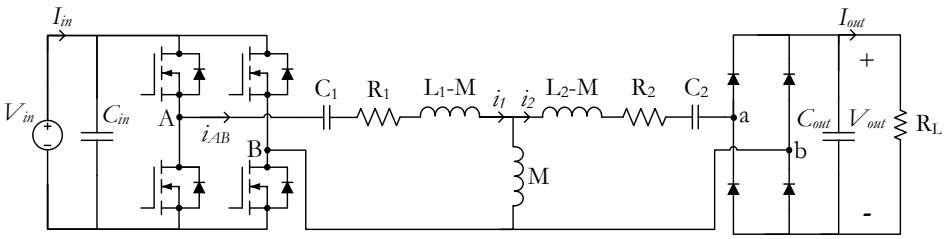

Figure 2.14: The equivalent model of a Series-Series compensation network.

The rectifier and load can be modeled as a resistor R_{AC} given by (2.12) [16].

$$R_{AC} = \frac{8}{\pi^2} R_L \tag{2.12}$$

The peak voltage of the first harmonic component of the inverter's square waveform voltage is used in this analysis, which is:

$$\hat{V}_{AB} = \frac{4}{\pi} V_{in} \tag{2.13}$$

Moreover the source and load current are given by:

$$I_{in} = \frac{2}{\pi} \hat{I}_1 \tag{2.14}$$

$$I_{out} = \frac{2}{\pi} \hat{I}_2 \tag{2.15}$$

Furthermore, the peak current is also used. The following equations can be derived by using Kirchhoff's and Ohm's laws on the equivalent model:

$$\hat{V}_{AB} = z_1 \hat{I}_1 + j\omega M(\hat{I}_1 - \hat{I}_2) \tag{2.16}$$

$$z_2 \hat{I}_2 = j\omega M(\hat{I}_1 - \hat{I}_2) \tag{2.17}$$

With

$$z_1 = R_1 + j\left(\omega(L_1 - M) - \frac{1}{\omega C_1}\right) \tag{2.18}$$

$$z_2 = R_2 + R_{AC} + j\left(\omega(L_2 - M) - \frac{1}{\omega C_2}\right) \tag{2.19}$$

The current gain G_i can be derived from (2.17).

$$G_i = \frac{|\hat{I}_2|}{|\hat{I}_1|} = \frac{|j\omega M|}{|z_2 + j\omega M|} \tag{2.20}$$

The voltage gain G_v is given by combining (2.16), (2.17) and multiplying it with R_{AC}:

$$G_v = \frac{|R_{AC}\hat{I}_2|}{|\hat{V}_{AB}|} = \frac{|j\omega M R_{AC}|}{|z_1 z_2 + j\omega M(z_1 + z_2)|} \tag{2.21}$$

The voltage and current gain are plotted in Figure 2.15 and Figure 2.16.

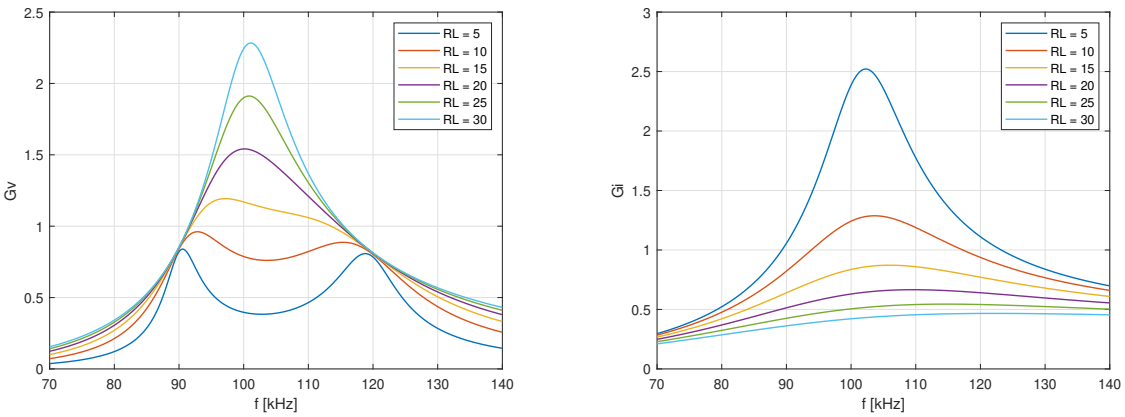

(a) (b)

Figure 2.15: (a) Voltage gain and (b) Current gain for different loads with k = 0.28.

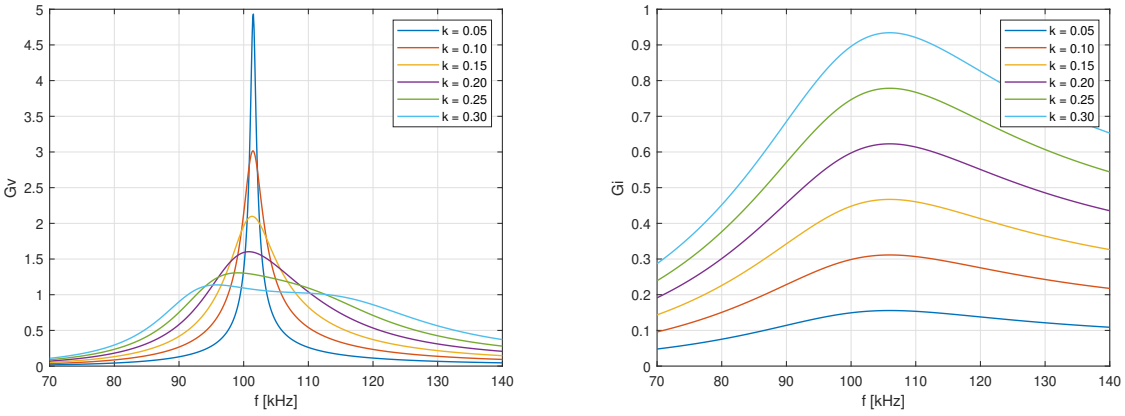

(a) (b)

Figure 2.16: (a) Voltage gain and (b) Current gain for different k with R_{load} = 15 Ω.

The voltage gain has a maximum at the resonance frequency for higher loads and lower coupling factors. For lower loads and higher coupling factors, the maximum of the voltage gain starts to shift in two local maximums. These two local maximums are at the frequencies where bifurcation would take place. This is observed by comparing Figure 2.13(b) and 2.15(a). This means that the maximum will not be at the resonance frequency.

The efficiency and power factor of the series-series compensation network can be calculated by:

$$\eta_{SS} = G_v G_i \tag{2.22}$$

$$PF = cos[Phase(Z_{in})] \tag{2.23}$$

The results of the efficiency and power factor are plotted in Figure 2.17 and Figure 2.18.

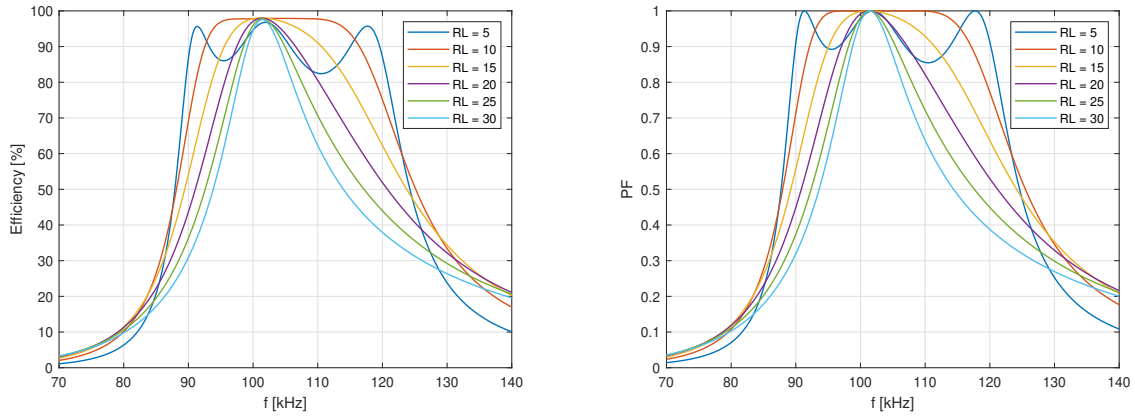

(a) (b)

Figure 2.17: (a) Efficiency and (b) Power Factor for different loads with k = 0.28.

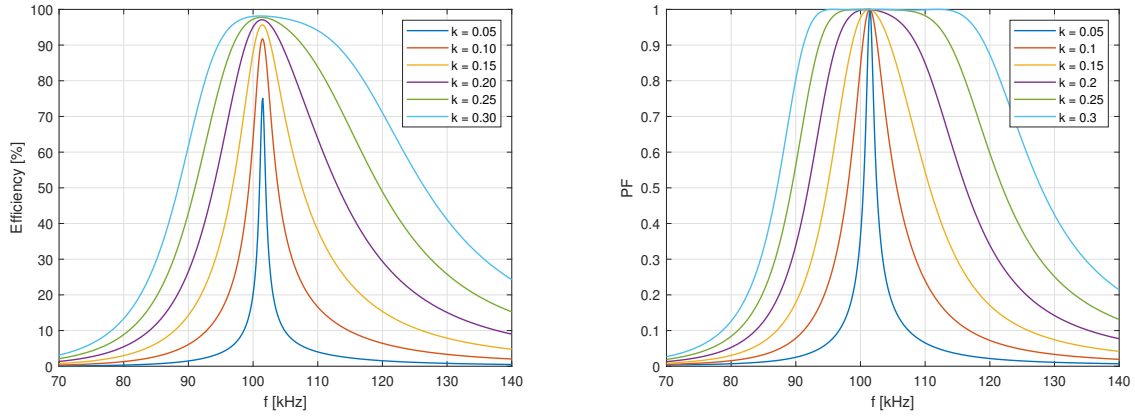

(a) (b)

Figure 2.18: (a) Efficiency and (b) Power Factor for different k with R_{load} = 15.

The efficiency has maximums at the resonance frequency, however for low loads it is possible that there are multiple maximums. From Figure 2.18 it can be observed that a higher coupling factor gives a better efficiency. This shows that it is really important to avoid misalignment as this would reduce the coupling between the coils, which results in less efficiency. The efficiency does not differ as much for the change in load resistance. The efficiencies at the resonance frequencies for different loads are shown in Table 2.3.

Table 2.3: The efficiencies at the resonance frequency for different loads.

R_L	Efficiency [%]
5	96.79
10	97.89
15	98.02
20	97.95
25	97.77
30	97.54

The efficiencies only differ a few percents of each other and the efficiency is at its highest for a load of 15 Ω. The inverse of the current gain at the resonance frequency if R_2 is neglected. This will give:

$$\frac{|\hat{I}_1|}{|\hat{I}_2|} = \frac{R_{AC}}{\omega_0 M} \tag{2.24}$$

The losses are minimal when:

$$\frac{d}{dR_{AC}}\left(\frac{R_2\hat{I}_2^2 + R_1\hat{I}_1^2}{R_{AC}\hat{I}_2^2}\right) = 0 \tag{2.25}$$

By substituting (2.24) into (2.25) it is possible to compute the optimal value for R_{AC} as given in (2.26). The load resistance of 15Ω is the closest to the optimal load resistance which is the reason why it has the highest efficiency at the resonance frequency.

$$R_{AC,opt} = \omega_0 M\sqrt{\frac{R_2}{R_1}} \tag{2.26}$$

2.3. Coil Topologies

The coils in a WPT system enables the system to transfer power in a wireless manner which makes them one of the most important components in the system. The work principle is explained by Ampère's and Faraday's laws describing the transfer power from the primary to the secondary coil [4]. The laws can be described in the following way.

1. Ampère's Law: A conductor that carries a current I produces a magnetic field H. Where the displacement current I_d is ignored for good conductors [17].

$$\oint_C \boldsymbol{H}\,d\boldsymbol{l} = \boldsymbol{I} + \boldsymbol{I_d} \tag{2.27}$$

2. Faraday's Law: An electric current is induced in a conductor if it is linked with a time varying magnetic flux [17].

$$\oint_C \boldsymbol{E}\,d\boldsymbol{l} = -\frac{\delta\boldsymbol{\phi}}{\delta t} \tag{2.28}$$

This chapter explains the advantages and disadvantages of the following five known coil topologies:

- Circular Pad
- Rectangular Pad
- Flux Pipe
- DD Coil
- Bipolar Pad

2.3.1. Circular Pad

The circular pad in Figure 2.19 is one of the most commonly used coil structures. The reason why it is so commonly used is because of its single-sided magnetic field. This will reduce the leakage flux that can be reduced further with the help of shielding. The shielding of circular coils is a necessity to achieve a high coupling coefficient and better misalignment tolerance [4]. Moreover, the leakage flux is reduced especially when used for EVs due to the steel floor pan [18]. However, the circular coil has a "dead zone" where no power will be transferred if it deviates at least 40% from the center [18].

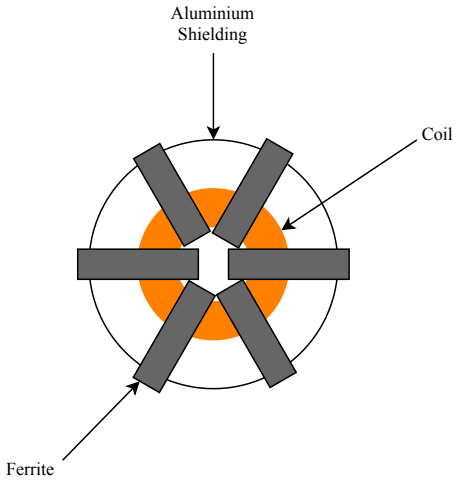

Figure 2.19: Circular pad.

2.3.2. Rectangular Pad

The rectangular pad in Figure 2.20 shows a similar behaviour as the circular pad. The difference is that the rectangular pad has a lower coupling coefficient when the primary and secondary are aligned when they have similar dimensions [19], [20]. However, the rectangular pad loses less coupling with misalignment in the lateral direction [19]. This has to do with the geometry of the ferrite. The magnetic field is shaped in lateral direction for the rectangular pad. While, for the circular pad it is shaped in a more vertical direction.

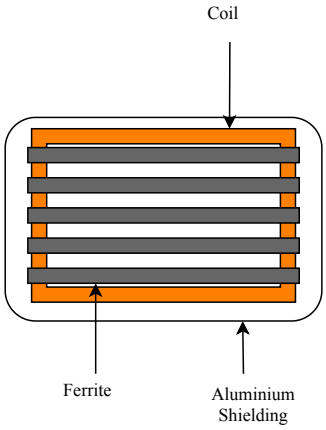

Figure 2.20: Rectangular pad.

2.3.3. Flux Pipe

The flux pipe is shown in Figure 2.21, the design is a ferrite core with two coils wounded along it. The advantages of this structure over a circular pad are higher misalignment tolerance and higher coupling coefficient if not shielded [21]. The problem occurs when the flux pipe is shielded because the shielding will catch flux from one side of the coil due to its solenoidal shape [4].

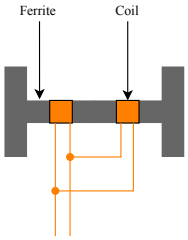

Figure 2.21: Flux pipe.

2.3.4. DD Coil

The DD coil in Figure 2.22 is a combination of the circular pad and the flux pipe. It consists of two coils which are magnetically connected in series. The ferrite is placed underneath the coil on top of the shielding. This allows for no losses in the quality factor. The DD coil still has a "dead zone" just like the circular pad, but this could be solved by adding a quadrature coil [18]. The DD coil has better a coupling factor than the circular pad and better misalignment tolerance than the circular pad. However this only applies for a larger misalignment. There will be more leakage flux close to the center of the DD coil in comparison to the circular pad [18].

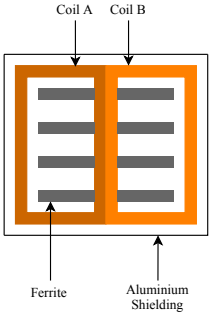

Figure 2.22: DD coil.

2.3.5. Bipolar Pad

The bipolar pad is similar to the DD coil except that the two coils have an overlap as shown in Figure 2.23. The partial overlap of the two coils avoids the interaction between the two coils which results in independence of the fields generated by each coils [22]. The performance of the bipolar pad is similar to the DD coil with quadrature coil [22], [23]. However, it has as an advantage that it needs less copper [22]. Furthermore, the performance of the bipolar pad reduces by adding an aluminum shield. It results in a reduced coupling coefficient because the magnetic flux is double-sided which will block one of the sides [4].

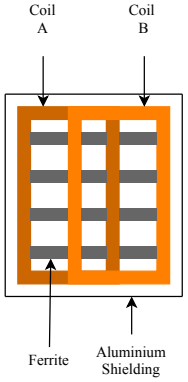

Figure 2.23: Bipolar pad.

A trade-off table is made for the discussed coil topologies in Table 2.4. This table shows that the bipolar

pad outperforms all the other coils in misalignment tolerance and coupling. However, its double-sided magnetic flux behavior limits its performance with an aluminum shield. Furthermore, circular and rectangular pads have single-sided magnetic flux behavior which allows them to outperform the bipolar pad if aluminum shielding is used [4]. So, it is important to take these characteristics into consideration when choosing the coil topology.

Table 2.4: Trade-off table for the different coil topologies.

Coil topology	Misalignment tolerance	Coupling coefficient when aligned	Influence of shielding	Magnetic flux
Circular pad	-	+-	Better misalignment tolerance and coupling coefficient	Single-sided
Rectangular pad	+-	-	Better misalignment tolerance and coupling coefficient	Single-sided
Flux pipe	+-	+-	Sensitivity to the flux from the other side which reduces coupling	Double-sided
DD coil	+-	+-	Higher coils' quality factor	Double-sided
Bipolar pad	+	+	Lower coupling factor (only for aluminum shield)	Double-sided

2.4. Standards

With the rise in popularity of EVs, it is essential to have standards to regulate EV charging though WPT. This will ensure safer systems and better interoperability between different parties. A short introduction is given about each one of the three standards that are currently available for the public.

2.4.1. IEC 61980-1

This standard is involved with common aspects for all power transfer technologies like use cases, electrical safety, electromagnetic compatibility (EMC) and electromagnetic field exposure (EMF) [24]. The EMC requirements for immunity and conducted disturbances are based on the well-known standards part of the IEC 61000 series. The EMF exposure of humans limits are based of ICNIRP from the IEEE or of national regulations. The limits in the Table 2.5 only apply for the area around the vehicle and inside the vehicle. The requirement regarding the harmonics is the most important thing related to the control because soft-switching can reduce these harmonics. This will be further elaborated on in Chapter 2.4.4.

Table 2.5: EMF exposure limits in the frequency range 3kHz-10MHz (RMS values) [25].

Electric field strength [V/m]	Magnetic field strength [A/m]	Magnetic flux density [μT]	Contact current [mA]
83	21.5	27	0.2*f[kHz] = 17 @ 85kHz

2.4.2. ISO 19363

This standard includes the requirements for safety and interoperability for magnetic field power transfer for passenger cars and light duty vehicles [7]. It has some shared parts with IEC 61980-1. It has a specification where it defines different power classes and Z-classes, where IEC 61980-3 has to confirm the power level and interopability of these classes. However IEC 61980-3 is still in development.

The standard also includes some efficiency and operating frequency requirements. The WPT system should have a minimum efficiency of 85 % at with no misalignment and a minimum efficiency of 80 % at the maximum allowed misalignment. The operating frequency range is found within 81.38 to 90 kHz with a nominal frequency of 85 kHz.

It does not have any EMC regulations of its own as these are referred to CISPR/D which is currently in development. The standard has two different protection levels for EMF. One of the levels is based of ICNIRP Guideline 2010 and the other one of ISO 14117-1. The one based of ICNIRP Guideline 2010 is a general limit to protect humans from electromagnetic fields, while the one based on ISO 14117-1 is there to keep the functionality of active implantable medical devices secure.

2.4.3. SAE J2954 RP

This standard provides technical guidelines and references for light-weight EVs which work with stationarity and unidirectional WPT charging [26]. Currently, there is a certain compatibility between transmitter system and depending on the power class or z-class of the receiver side. Furthermore, there are references that include offset tolerances for EV misalignment. The operating frequency should be between the 79 and 90 kHz with a nominal frequency of 85kHz. The EMC limit is 67.8 dB for WPT1 and WPT2. For WPT3 is 82.8 dB. The general limit for EMF is also based of ICNIRP Guideline 2010, just like in ISO 19363. The EMF for active implantable medical devices are based of AAMI/ISO 14117-2012.

The standard also includes regulations for foreign object detection and living beings protection. The power transfer process will be stopped in the case that a foreign object is detected. Additionally in the case no object is detected, then the temperature of the transmitter side should be monitored and should not exceed a set limit. Moreover it should be able to detect a living being within its vicinity and act fast enough to ensure that the radiated field is not a hazard.

Furthermore, efficiency targets are set for different power levels. In Table 2.6 the efficiency requirements are shown. The requirements for WPT4 still need to be decided upon. Moreover, an efficiency of 75% is required for power classes that are not listed in this table. This gives an example of why it is of importance to have soft-switching for the inverter as it could help the system to reach more easily the listed efficiency requirement from this standard by reducing the switching losses in the inverter.

Table 2.6: Efficiency requirements for different power levels for WPT [26].

	WPT Power Class			
	WPT1	WPT2	WPT3	WPT4
Maximum input VA	3.7 kVA	7.7 kVA	11.1 kVA	22 kVA
Minimum target efficiency at nominal X,Y alignment	>85%	>85%	>85%	TBD in next phase
Minimum target efficiency at offset position	>80%	>80%	>80%	TBD in next phase

2.4.4. Comparison of EMC and EMF regulations

There are some differences between the regulations for EMC and EMF. It turns out that the electromagnetic field strength limits for EMC according to IEC 61980-1 are only defined for frequencies above 150kHz, while SAE J2954 RP also defined limits below 150kHz as shown in Figure 2.24. IEC 61980-1 defines the magnetic field limits for frequencies below 150kHz, but they are only EMF related. The EMC limits are focused on electronic devices while the EMF limits are focused on human exposure. This can be observed in Figure 2.24 as the EMC limits are for a distance of 10m [27]. As proposed in [27], it would be better to define a unique limit which is valid for both. This would make the required operation limits more concrete.

However, it is noted that at around 20MHz the two standards start to have a similar trend. Without soft-switching, more harmonics would be present in the inverted voltage waveform. The square wave comprises already a sum of several harmonics, but the ringing created by the lack of soft-switching would make this even worse. The high-frequency harmonics would increase the magnetic field strength at very high frequencies, e.g. MHz range, that could result in not reaching the requirements of neither standards.

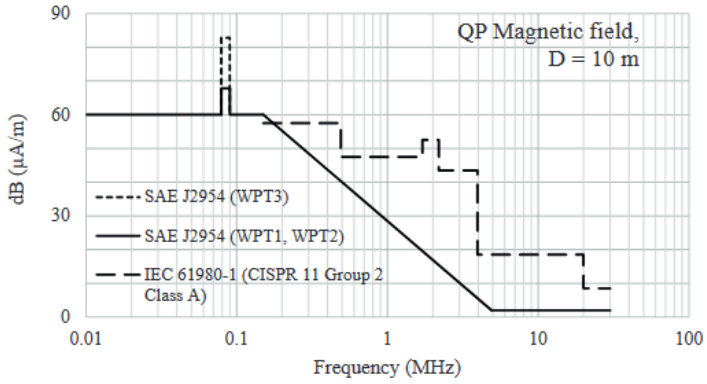

Figure 2.24: Limits of the magnetic field strength at 10m [27].

2.5. Control

To keep the WPT system as efficient as possible, it is necessary to minimize the losses at each part of system. There are different implementation strategies to realize different control methods. This chapter gives an overview of the different control methods with their trade-offs, and how these methods are implemented in WPT systems.

2.5.1. Phase Shift Control

This control scheme makes use of a constant switching frequency, but the phase shift α between switch pair S_1, S_4 and S_2, S_3 is varied as shown in Figure 2.25(b). This results in a symmetrical phase-shift control. Varying the phase-shift between the two pairs will give a different amplitude for the fundamental of the output voltage. Unfortunately bifurcation could occur which would make it harder to make soft-switching work. This would result in more switching losses due to reverse recovery of the diodes [28]. Likewise, to keep the power through the coils the same, it is required to increase the current at the primary side as the output voltage of the inverter decreases due to the phase-shift. By increasing the primary current, it will result in higher conduction losses [28]. There is also an asymmetrical phase-shift control as shown in Figure 2.25(c). It is an alternative method to introduce soft-switching to the inverter. It is shown in [29] and [30] that achieving soft-switching with this strategy is simpler than symmetrical phase-shift control.

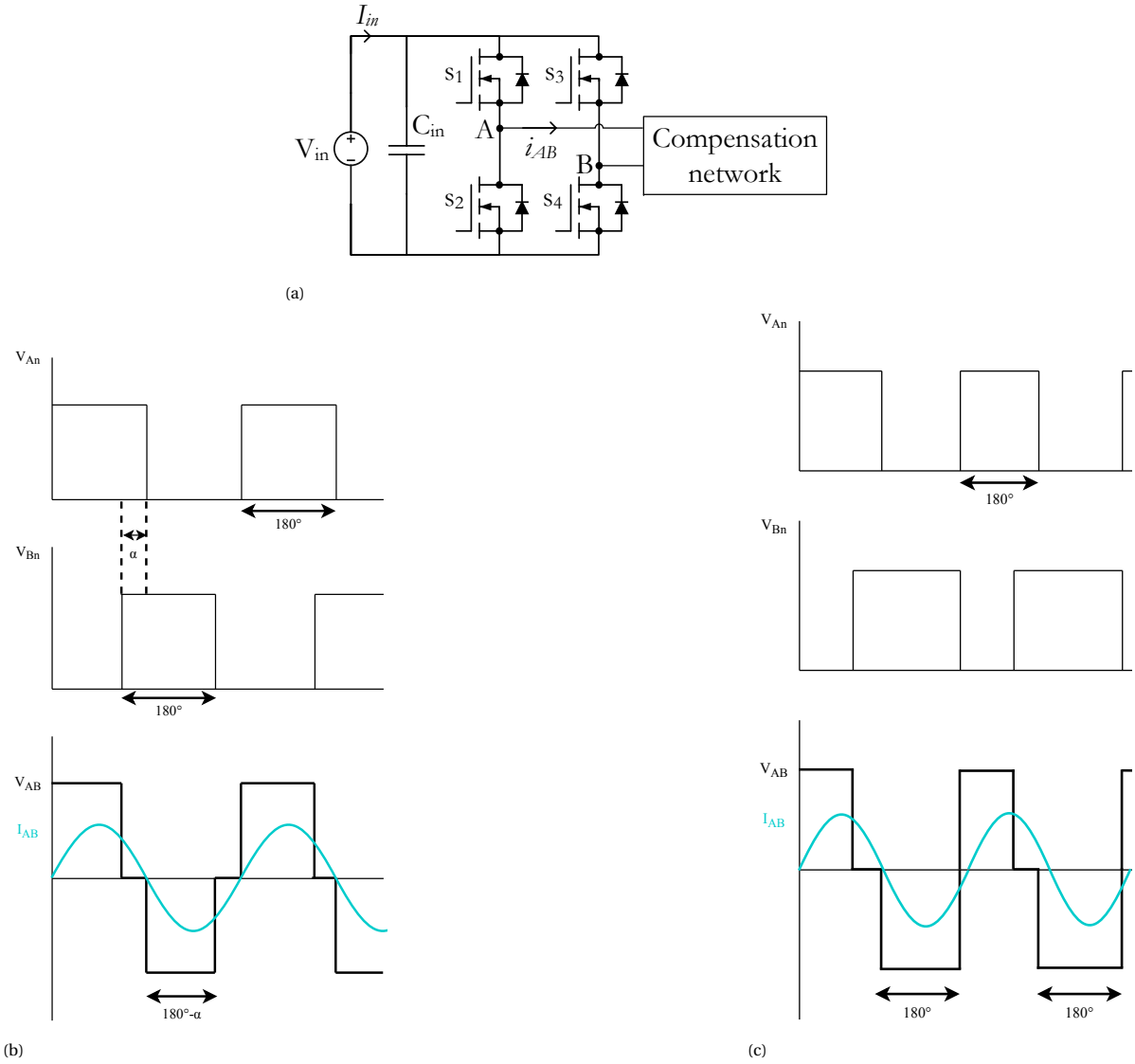

Figure 2.25: (a) Full-bridge inverter, (b) waveform with symmetrical phase-shift α and (c) asymmetrical phase-shift.

2.5.2. Frequency Control

In frequency control, the transmitted power is regulated by changing the frequency above the resonant frequency as shown in Figure 2.26. This happens because of the change in input impedance of the compensation network [28, 31, 32]. The disadvantage of using this control scheme is that it is susceptible to sudden changes in coupling and load [28]. Therefore hard-switching could happen. This means that constant monitoring is necessary for this control scheme.

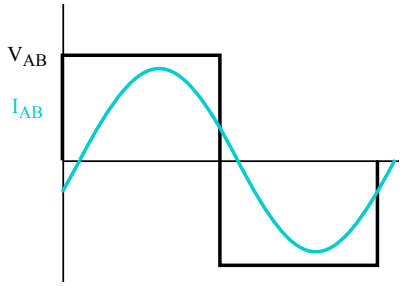

Figure 2.26: Output voltage and current of the inverter with frequency control.

2.5.3. Dual Control

By combining phase-shift and frequency control it is possible to obtain another control scheme: dual control. The frequency is controlled by detecting the zero-crossing current in the primary coil. This will guarantee that the switching frequency is equal to the resonance frequency [28]. The output of the inverter will look like the one in Figure 2.27.

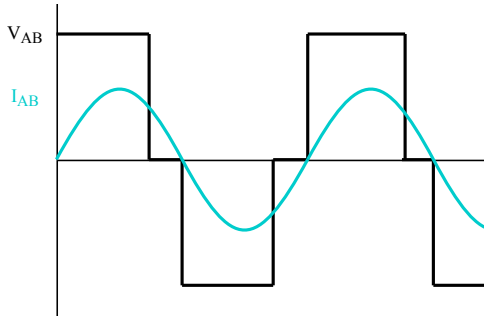

Figure 2.27: The output voltage with fundamental and output current of a dual controlled inverter.

It is also possible to keep the input power constant in case the primary current changes due to a change in coupling factor.

2.5.4. Impedance Matching

As described in [4] and [33], this control method keeps the switching frequency close to the resonance frequency. Moreover the DC output voltage to charge the battery and the DC input voltage of the inverter should be adjusted to ensure maximum efficiency of the coils at the chosen power level.

The output power for an WPT system using a series-series compensation network is given by [33]:

$$P_{out} = \frac{8}{\pi^2} \frac{V_{in} V_{out}}{\omega_0 M} \tag{2.29}$$

Therefore, it is possible to meet the required P_{out} by controlling V_{in}.

According to [16] the equivalent AC resistance of the secondary-side is:

$$R_{ac} = \frac{8}{\pi^2} \frac{V_{out}^2}{P_{out}} \tag{2.30}$$

It is possible to match the load to maximize the efficiency. In the case for a series-series compensation network at resonance frequency it is given by (2.26).

Combining (2.26) and (2.30) gives:

$$V_{out} = \sqrt{\frac{\pi^2}{8}\omega_0 M P_{out}\sqrt{\frac{R_2}{R_1}}} \tag{2.31}$$

So the output voltage of the secondary-side from (2.31) is adjusted to match the optimum equivalent load that maximizes the coils' efficiency. This could be managed by a buck-boost converter at both primary and secondary sides.

By using the optimal impedance it is possible to attain higher efficiencies. However the efficiency could be reduced because of the extra DC-DC converter used. This would also mean that more space is necessary for the WPT system.

2.5.5. Main feedback control implementations

Generally, impedance matching is done as in Figure 2.28. As told in Chapter 2.5.4, this is generally done by controlling the voltage at the primary and secondary sides. In [34], an FPGA controller is used to monitor the voltages and currents and to control the system. The voltage at the load is adjusted by an active rectifier while the voltage at the primary side is adjusted using phase-shift control at the inverter. This phase-shift is determined by the phase-shift at the active rectifier, the measured battery voltage, the measured DC link voltage of the primary side and the desired nominal values of the DC link voltage.

However, in [6], [35] and [36], an extra DC/DC converter is used after the rectifier to match the impedance instead of the active rectifier. This would come with the trade-off of more components and space, but it is possible to use simpler control.

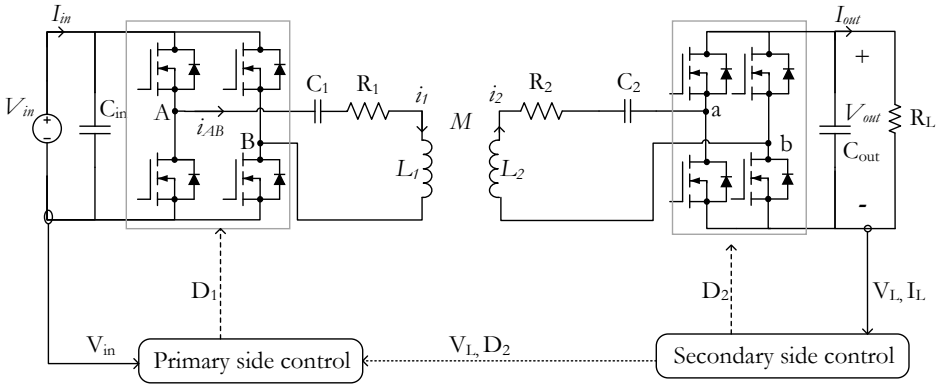

Figure 2.28: Control diagram of [34].

The dual control is typically performed such as in Figure 2.29. The zero-crossing in the primary side current is detected from which the resonance frequency is determined. Afterward, a controller is used to adapt to these frequencies and set the phase-shift. In [37], several logic gates and comparators are used to detect the zero-crossing and to control the gate-outputs.

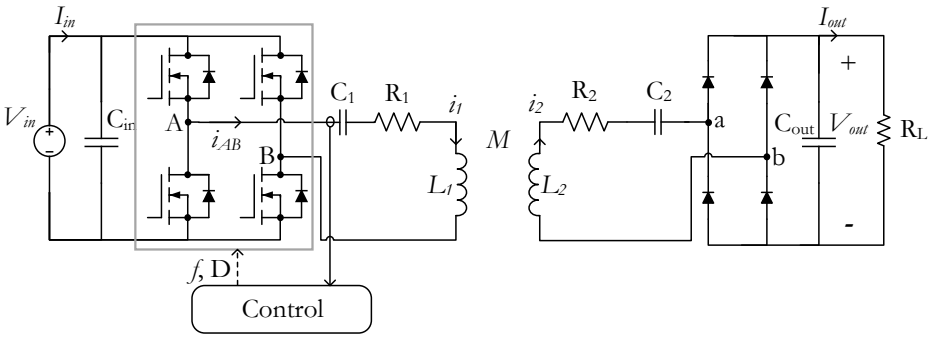

Figure 2.29: General control diagram of dual control.

In [33], [38] and [39] a digital controller is used in combination with some zero-crossing detectors. This would allow for a controller with more functionalities. It is easier to do certain tasks such as start-up, shut-down, protection of the circuitry and frequency limitation. Furthermore, it would allow the controller to do more complex control as for example computing the efficiency of the WPT system [6], [36], [40], [41]. However, analog control allows for faster actions and is overall cheaper.

Additionally most controllers make use of communication between the primary and secondary side due to the need to exchange data between those sides. Some of the used communication methods include WLAN [36], TCP/IP [39] and DSRC [41]. Lastly all implementations control the primary side to ensure soft-switching at the inverter.

3

Digital Control

The objective of the inverter control is to guarantee that the WPT system can efficiently and safely charge the EV batteries for all operating ranges and conditions the hardware is designed for. This includes the safe start-up and shutdown of the system, the circuit component protections, and above all to ensure soft-switching of the semiconductors for the maximization of power efficiency. Digital control grants more functionalities than analog control. However, analog control is still a necessity due to the relatively high switching frequency operation. The digital control would be too slow, so it should be integrated with an analog logic control with a high bandwidth sensing.

First, an open-loop controller is designed which can set the frequency and dead time of the H-bridge inverter. Then, it will be tested on an existing e-Bike wireless charging setup at low power to test the ZVS capabilities of the controller. Afterward, the closed-loop controller is designed. It should consist of the following features of the soft start-up, soft shut-down and over-current protection at the primary side.

3.1. Laboratory Prototypes used for the Proof of Concept

There are two WPT setups used for practical testing. The first one is the 200W e-bike setup which circuit schematic is shown in Figure 3.1, and the component values are shown in Table 3.1. The second prototype is composed of 2.5kW EV charging coils which have been connected to both series-series and double-sided LCC compensations as shown in Figure 3.2(a) and 3.2(b). Both configurations have been designed for an output power of 1.1kW, and the components' values are displayed in Table 3.2.

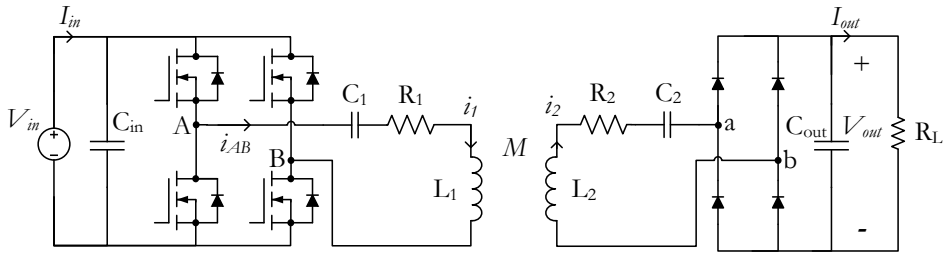

Figure 3.1: The 200W e-bike wireless charging setup.

Table 3.1: The values used for the open-loop controller test.

Parameter	Value [unit]
L_1	57.05 [μH]
L_2	50.53 [μH]
C_1	57.8 [nF]
C_2	68.0 [nF]
R_L	14.7 [Ω]
k_{max}	0.26 []

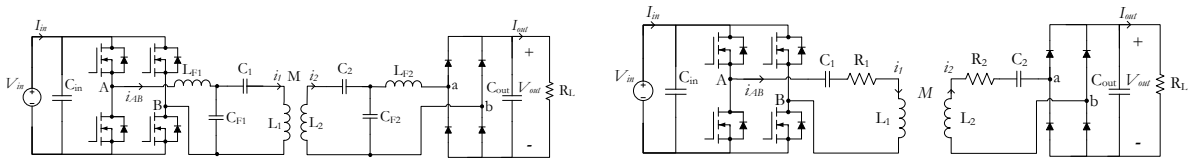

(a) (b)

Figure 3.2: The 1.1kW WPT setup with: (a) double-sided LCC compensation network, and (b) series-series compensation network.

Table 3.2: Component values for the 1.1kW system.

	LCC	SS
L_1	202.5 [μH]	202.5 [μH]
L_2	204.4 [μH]	204.4 [μH]
L_{F1}	65.26 [μH]	N/A
L_{F2}	68.69 [μH]	N/A
C_1	25.55 [nF]	18.40 [nF]
C_2	28.7 [nF]	18.22 [nF]
C_{F1}	53.7 [nF]	N/A
C_{F2}	28.70 [nF]	N/A
R_L	145 [Ω]	15 [Ω]
k	0.1089	0.1089

3.2. Open-Loop Control

The open-loop controller sets the frequency and duty cycle of the inverter based on the user selection, without the need of a feedback signal. Moreover, the open-loop controller is designed to get accustomed with the programming of the controller and it is a first step into the design of the desired closed-loop controller.

The control is programmed on a C2000 Delfino MCU F28379D LaunchPad. It is possible to program the controller in Simulink with the Embedded Coder Support Package for Texas Instruments C2000 Processors (ECSPTIC2000) add-on provided by MathWorks. The controller will be able to set the frequency in the time-base and action qualifier sub-module and the dead time in the deadband module as shown in Figure 3.3. Besides, it will test the serial communication interface. The operation of the open-loop controller is tested with the inverter of the e-bike wireless charging setup from Chapter 3.1.

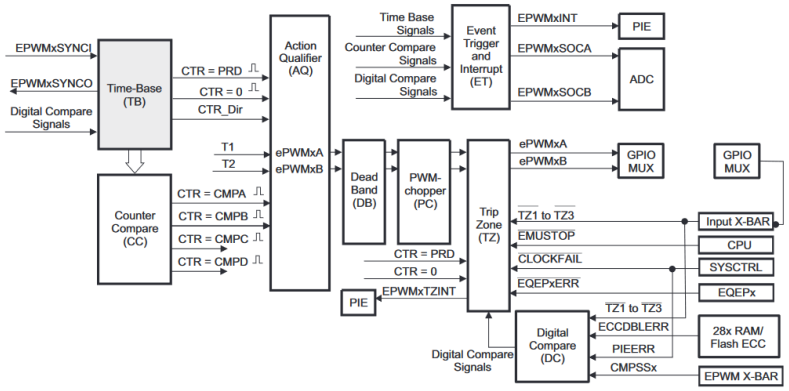

Figure 3.3: The ePWM module [42].

3.2.1. Programming of the open-loop controller

The host and main models are given in Figure 3.4 and Figure 3.5. The main model is converted into C/C++ code by the ECSPTIC2000 to make it possible for the launchpad to be programmed. The function of the host model is to change the frequency and deadband of the main model while it is running on the launchpad. When the main model is programmed correctly onto the launchpad only a blue led should blink.

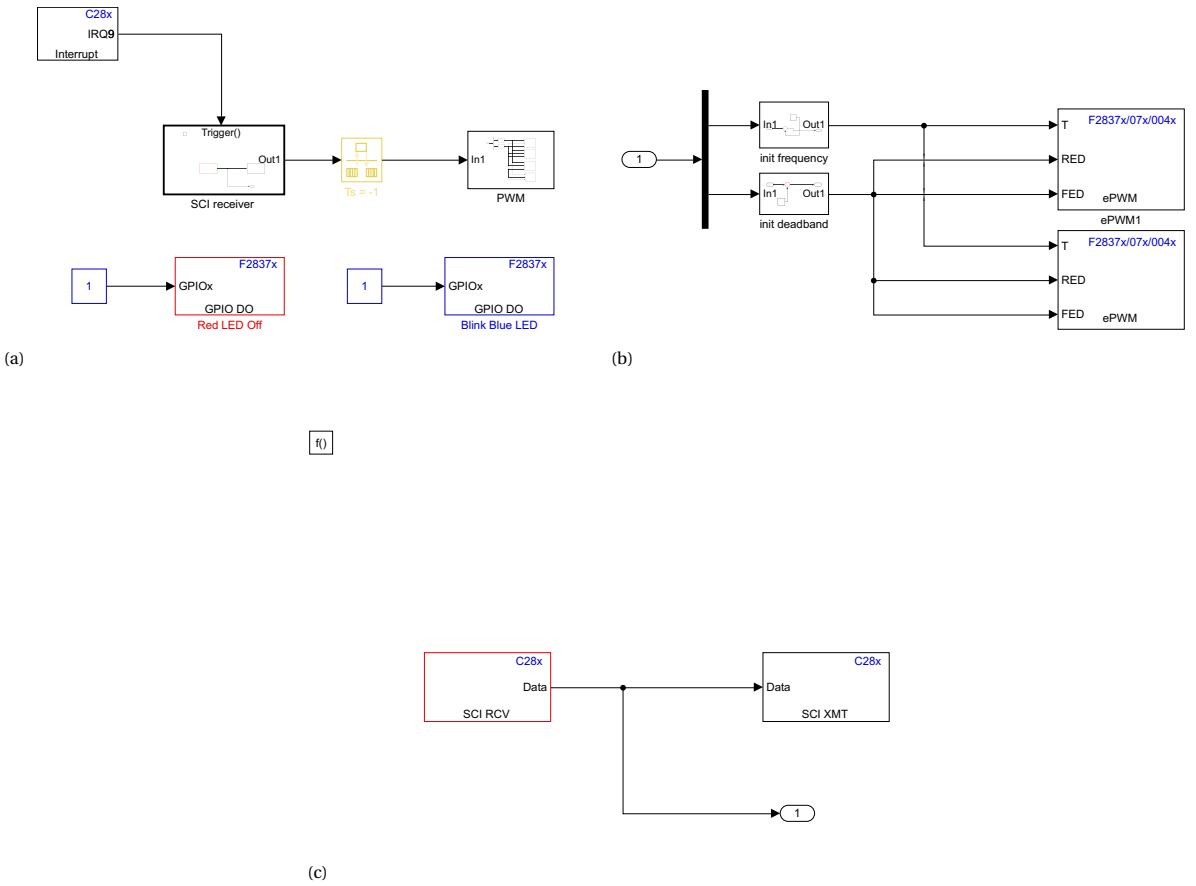

Figure 3.4: (a) Main model, (b) PWM subsystem and (c) Serial Communication Interface (SCI) subsystem of the open-loop controller.

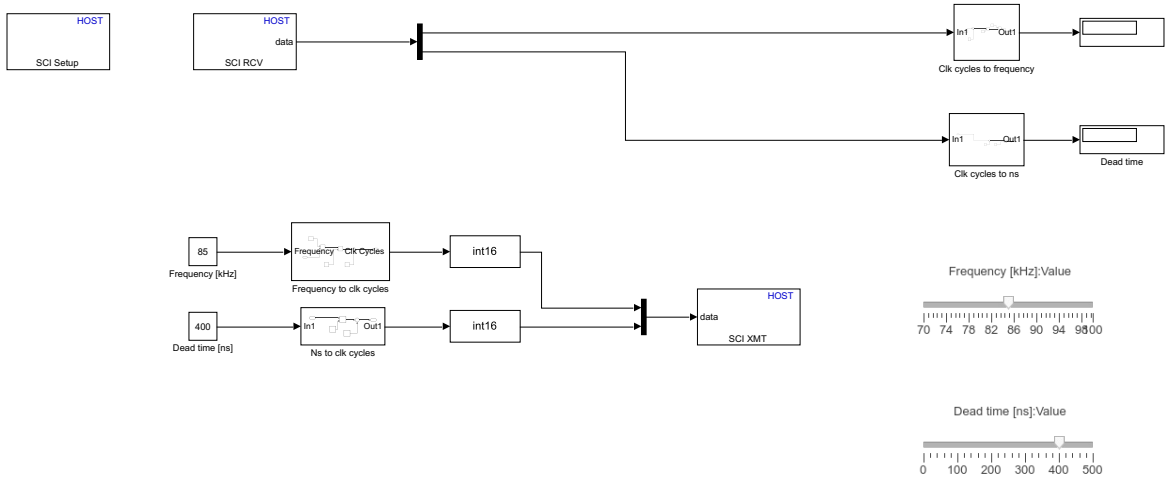

Figure 3.5: Host model.

The PWM subsystem in Figure 3.4b consists of four ePWM modules. Their counting modes are set on up-down-count mode to prevent the use of the action qualifier sub-module in Figure 3.3. When the counter = 0 or counter = prd, this would give a situation where the launchpad is not able to update the registers in time in case of a change in frequency. The time-base period in clock cycles for the ePWM module is calculated by [42]:

$$TBPRD = \frac{1}{2}\frac{f_{TBCLK}}{f_{PWM}} \tag{3.1}$$

where f_{TBCLK} is the frequency of the time-base clock and f_{PWM} is the desired PWM frequency.

The deadband submodule in Figure 3.3 will automatically change the duty cycle of the PWM signal in accordance with the requested deadband. The deadband in clock cycles is given by:

$$DB_{CLKCYCLES} = \frac{DB_{seconds}}{T_{TBCLK}} \tag{3.2}$$

Where $DB_{seconds}$ is the desired deadband in seconds and T_{TBCLK} is the period of the time-base clock. The two blocks: init frequency and init deadband will give a starting frequency and deadband to the ePWM modules. To synchronize both ePWM modules with each other, it is possible to use the synchronization output and synchronization action in the time-base submodule. The synchronization works much the same as the master-slave principle. One of the ePWM modules outputs a signal at the synchronization output when its counter reaches zero. The other ePWM modules have their synchronization action to count up with a phase-offset value because of the internal delay between the modules. The measured delay is about 20ns, so to compensate for the delay the phase-offset is set at 2 clock cycles as each clock cycle is 10ns. The serial communication of the SCI subsystem in Figure 3.4(c) makes it possible to change the frequency and deadband from the main model through the host model. Furthermore, the main model sends the received frequency and deadband back to the host model for verification. The hardware interrupt in Figure 3.4(a) makes sure that the changes in frequency and deadband are asynchronously from the system clock. This allows for fast and robust updates. The rate transmission block is mandatory to connect the asynchronous process of the serial communication and the synchronous process of the PWM subsystem.

3.2.2. Results of the open-loop controller

The output PWM signals are shown in Figure 3.6 and Figure 3.7. The switches from the left switching leg from Figure 3.8 is controlled by ePWMxA while the other leg is controlled by ePWMxB. The values from Table 3.1 and 3.3 are used for this experiment.

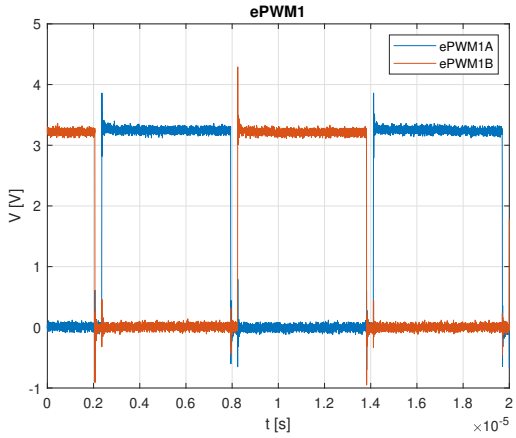

Figure 3.6: PWM output of ePWM1, frequency = 85kHz, deadband = 300ns.

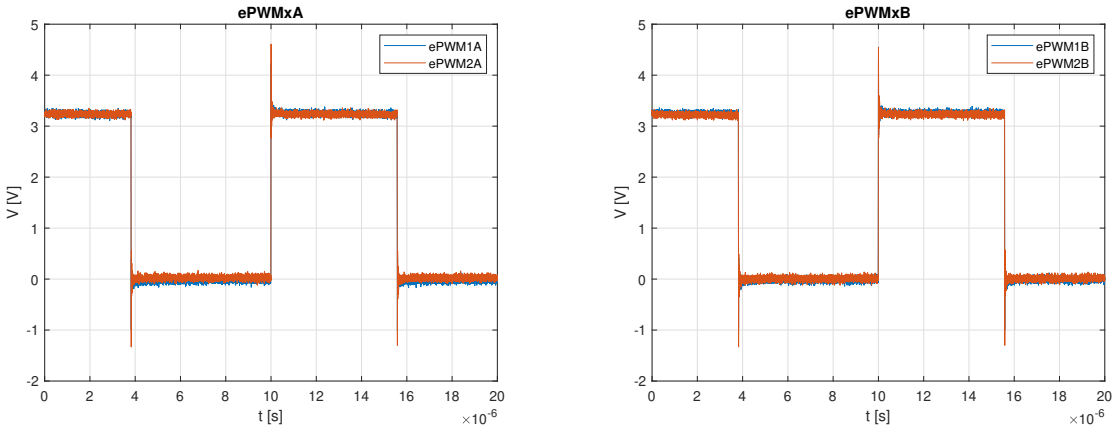

(a) (b)

Figure 3.7: Comparison of the PWM output for: (a) ePWMA and (b) ePWMB, frequency = 85kHz, deadband = 300ns.

It can be concluded from Figure 3.6 that the frequency and deadband give the specified value. Besides, in Figure 3.7 it is shown that all ePWM modules are synchronized with each other with minimal differences.

In Figure 3.8, the test results of the open-loop controller are shown, which have been measured from the e-bike WPT charging set-up.

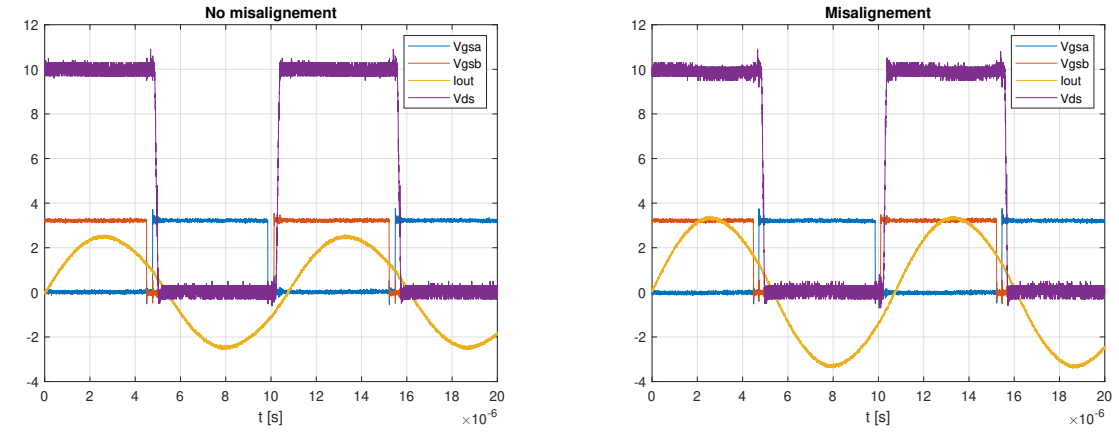

(a) (b)

Figure 3.8: ZVS of the inverter from the e-bike WPT charging set-up with: (a) no misalignment and (b) misalignment.

Table 3.3: Frequency and dead time settings.

	Frequency [kHz]	Dead time [ns]
Without misalignment	93.24	268
With misalignment	93.07	230

The results in Figure 3.8 shows that the voltage is leading the current which is necessary to achieve ZVS as mentioned in section 2.2.3. With misalignment, there are a bit more losses in the MOSFET which is due to the higher primary current. This happens because of the reduced coupling factor which is in line with what was proven in section 2.2.4.

3.3. Closed-Loop Control

The closed-loop control uses the output current of the inverter as feedback signal to regulate the switching frequency of the H-bridge inverter. This results in ZVS turn-ON that would follow the resonance. This is important as the tolerance of the component parameters could change the resonance frequency. Furthermore,

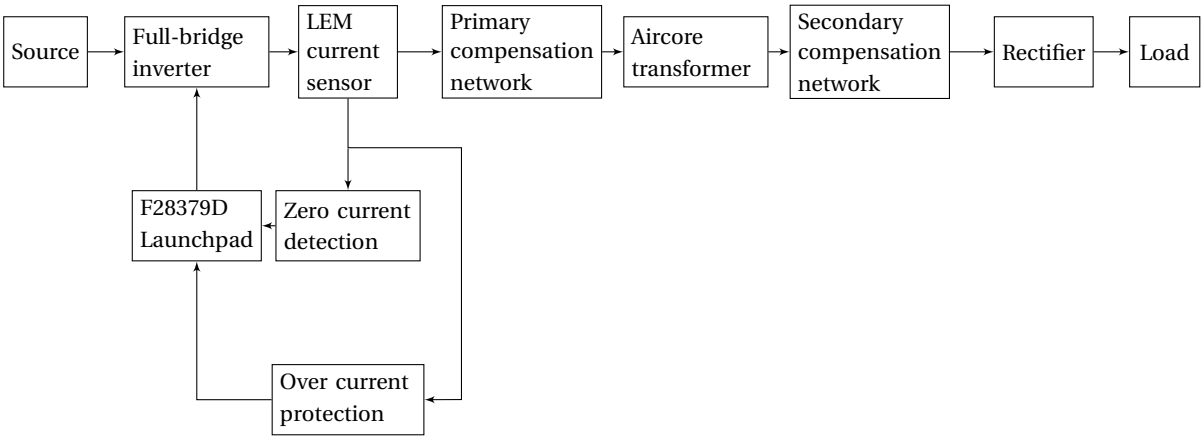

Figure 3.9: Block diagram of the whole system.

to follow the output current, an external analog based zero current detection (ZCD) circuit is used because of the necessary high resolution due to the relatively high switching frequency operation. Besides, over-current protection is used which, in case of a fault, trips the PWM signals coming from the F28379D launchpad. All these features that are shown in Figure 3.9 have been programmed in Simulink with the ECSPTIC2000 add-on from MathWorks, and tested in combination with the H-bridge inverter used in Figure 3.2.

3.3.1. Zero current detection

The zero current detection circuit is shown in Figure 3.10. The three main parts of the circuit are the comparator, AND gate and the rising edge D-type flip-flop.

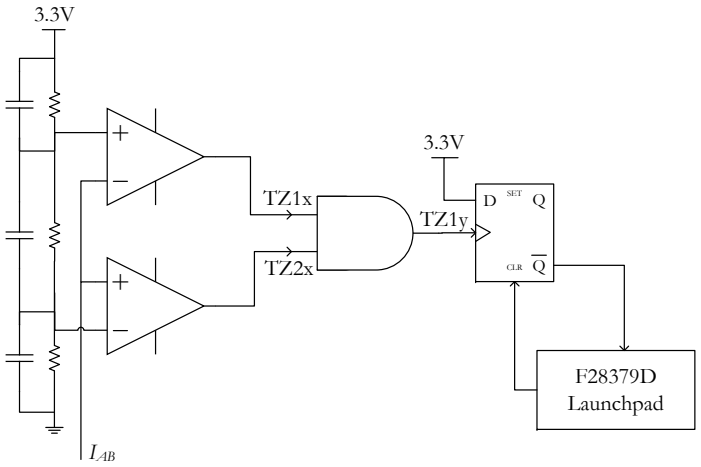

Figure 3.10: Simplified representation of the zero current detection of the inverter.

The references of the comparator are tuned by the resistors connected to the op-amps of the comparator. These will determine the position of the dotted red and green line in Figure 3.11. Afterwards, the comparator outputs TZ1x and TZ2x. These will go through an AND gate to form TZ1y, which is fed in the CLK input of the rising edge D-type flip-flop. Table 3.4 is made from the data-sheet of the flip-flop [43] and the inputs of the flip-flop from the design. This table shows that the outputs are dependent on only the CLR and TZ1y. The CLR is generated from TZ1y when TZ1y goes to a high state it will result in CLR going to a low state for a short time to reset the flip-flop output $\overline{Q}$. The output $\overline{Q}$ is taken as input from the LaunchPad as TZ1. Input TZ1 makes use of the tripzone submodule of the ePWM module. The tripzone is normally used for the protection as it has a very fast response which makes it a suitable to use for the zero current detection because of the relatively high switching frequency.

Table 3.4: Truth table of the rising edge D-type flip-flop [43].

CLR	CLK	Q	$\overline{Q}$
L	X	L	H
H	↑	H	L
H	L	Q_0	$\overline{Q_0}$

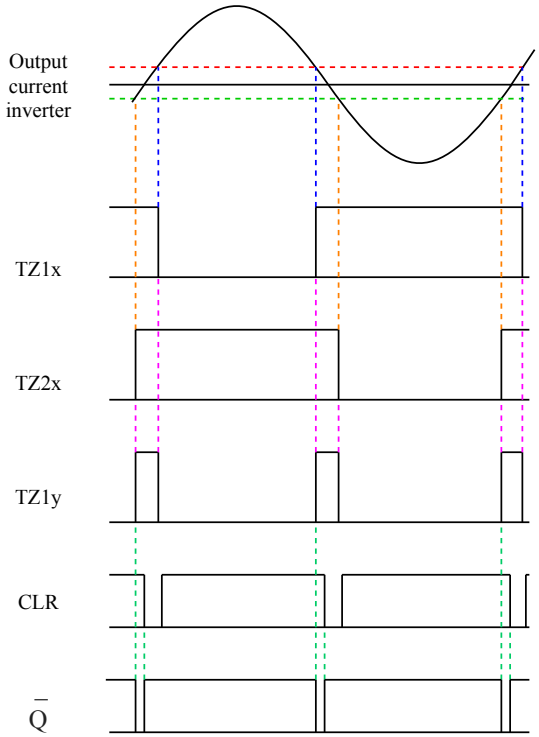

Figure 3.11: Signals of the zero current detection.

3.3.2. Over-current protection

The over-current detection is shown in Figure 3.12. It has a similar design as the zero current detection. The references of the comparator are tuned by the resistors in such a way that if the current is within the limits, it will output a high state at both outputs of the comparator. From Table 3.4, it can be derived that the output of the flip-flop ($\overline{Q}$) which is now referred to as TZ3 is high when the button is pressed to set the CLR low. Subsequently, the CLR goes back to high which will keep the last output state, so the output TZ3 stays high when no over-current is detected and the button should be pressed every time to reset the protection if an over-current happened. So, for normal operation TZ3 will be in a high state.

When an over-current occurs, it will have as a consequence that the output of the first AND gate will go to a low state. This would result in a rising edge at the CLK input of the flip-flop which brings the output TZ3 to a low state according to Table 3.4. This leads to the AND gate blocking the PWM signal which is going to the gate drivers. Additionally, the low state of TZ3 should also trigger the F28379D launchpad which set all the PWM signals to low as a back-up safety measure.

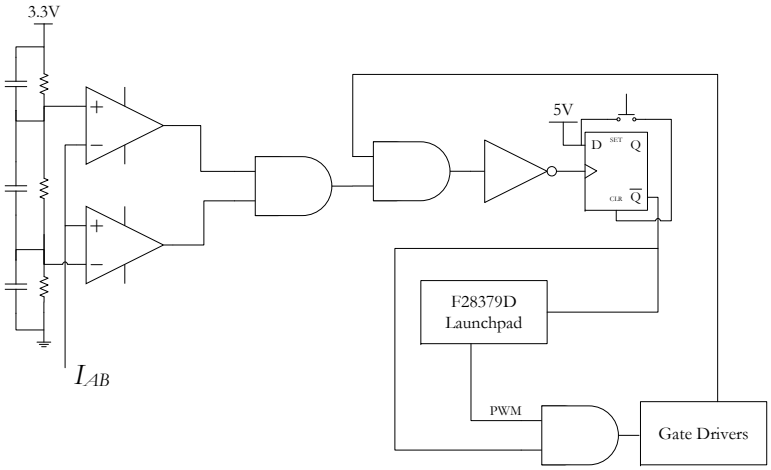

Figure 3.12: Simplified representation of the over-current protection of the inverter.

3.3.3. Programming of the closed-loop controller

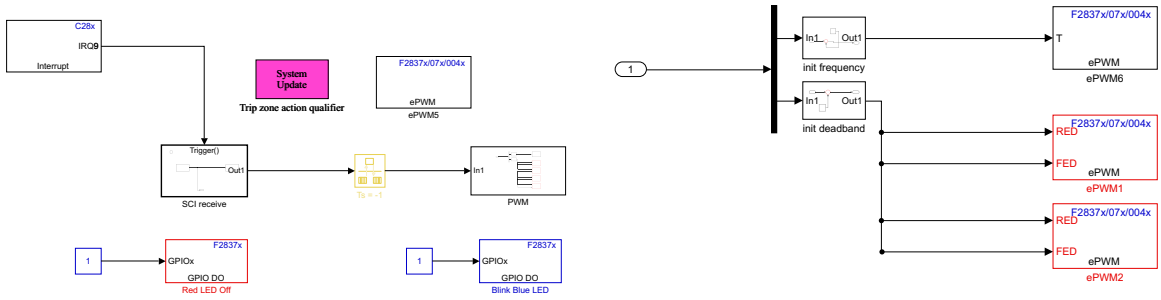

(a) (b)

Figure 3.13: (a) Main model and (b) ePWM unit of the closed-loop controller.

The designed controller is shown in Figure 3.13. The controller makes use of both the over-current protection and the zero-current detection cicuits. A similar host model is used to tune the frequency of ePWM6A and the deadband of ePWM1 and ePWM2, along with the same SCI subsystem as the open-loop controller. The current detection signal is replicated using ePWM6A. The deadband settings for ePWM1 and ePWM2 are identical to the deadband settings as in section 3.2.

Moreover, some extra code is added by the system update block in Figure 3.13a. This code is in Appendix A.1. This allows the use of the digital compare with the action qualifier. The digital compare signal (TZ1) is connected to the T1 input of the action qualifier. Every time TZ1 goes low, it will toggle ePWMxA and ePWMxB. This means that if the signal is in a low state, it will go to a high state and if the signal is in a high state, it will go to a low state.

Besides, the CLR signal is as well implemented with the help of the system update block. The CLR is made by ePWM5A and works in a comparably manner as the toggle for the other PWM signals. The time-base period is set very low in the ePWM module and it is set to go to a high state for the up and down count in the action qualifier. In the system update block code, it is programmed to go to a low state if TZ1y (TZ2) goes to a high state which creates the CLR signal from Figure 3.11.

Lastly, the protection is implemented by using the tripzone sub-module in Figure 3.3. The over-current protection signal (TZ3) will go to a low state in case of an over-current. The tripzone sub-module in all ePWM modules are set to do a one-shot trip for this case and set the output to low. The one-shot trip keeps this condition active until the F28379D launchpad gets a reset signal.

3.3.4. Results of the closed-loop controller

The PWM signals of the ePWM modules are measured and plotted in Figure 3.14-3.17. The over-current detection signal (TZ3) which is made by a function generator has to be in a high state to keep the ePWM modules functional. In Figure 3.14, it can be observed that V_{GS} and ePWM1B go to a low state if TZ3 also goes to a low state. The delay between V_{GS} and TZ3 is about 90ns. From Figure 3.15, it can be notices that ePWM1A and ePWM1B toggle at around the same moment as the falling edge of TZ1 in Figure 3.15. The delay is 64ns. Moreover, Figure 3.16 present the test of the zero-current detection with the logic of the PCB. It can be observed that the generated PWM signals fall around the time as the "dummy" measurement of V_{lem} reaches a zero crossing. The CLR is realized in Figure 3.17. It can be concluded that the CLR is generated in time as the delay is 66ns.

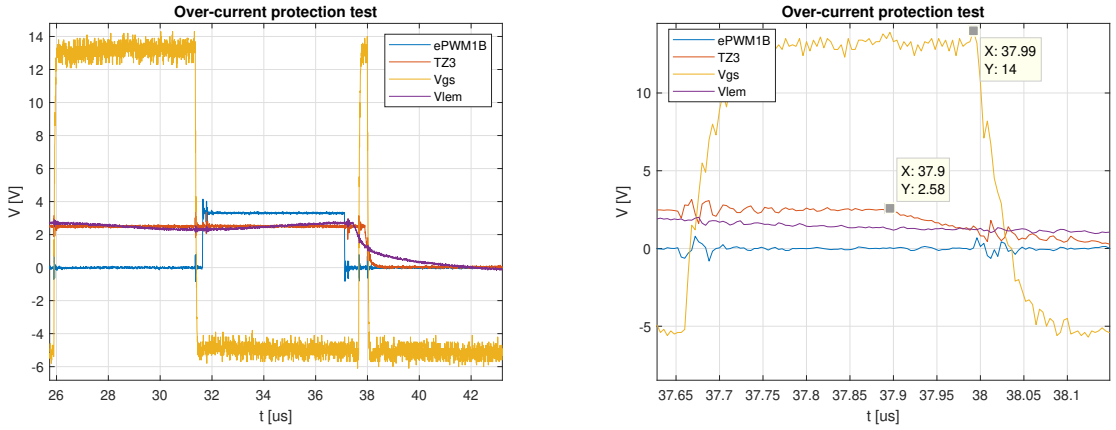

(a) (b)

Figure 3.14: The over-current protection test on ePWM1 normal version (a) and zoomed in version (b), frequency = 85kHz, deadband = 400ns.

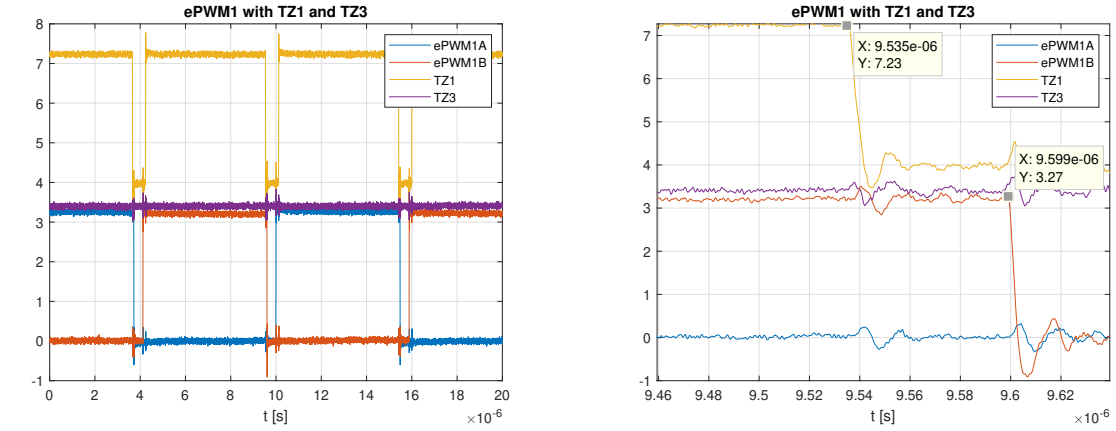

(a) (b)

Figure 3.15: The generated signals from ePWM1 with CLR and TZ3 (a) normal version and (b) zoomed in version, frequency = 85kHz, Deadband = 400ns.

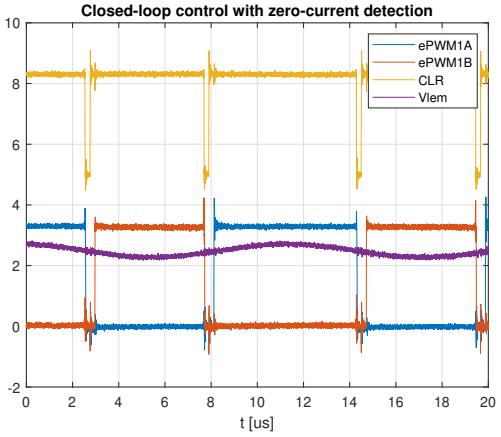

Figure 3.16: Zero-current detection test with the PCB, frequency = 85kHz, deadband = 400ns.

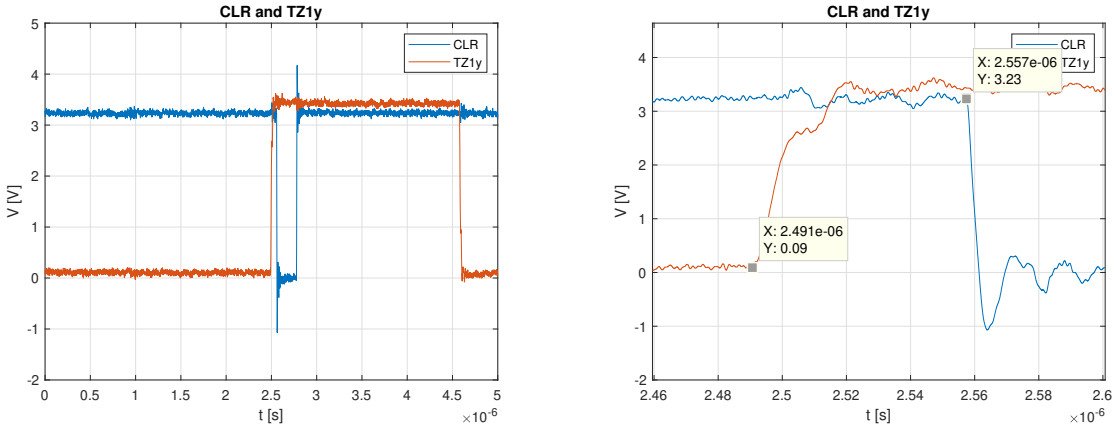

(a) (b)

Figure 3.17: The CLR for the rising edge D-type flip-flop and TZ1y (a) normal version and (b) zoomed in version.

3.4. Soft Start-up and Shut-down

During the start-up transient of the WPT, there would be a high output current from the inverter if the system starts at full power. This might damage the MOSFETs and could trip the over-current protection. The main challenge is to ensure soft-switching while ensuring safe operation of the WPT system. One of the solutions is shown in Figure 3.18. At the start-up, the controller would initially set the inverter to a frequency higher than the nominal resonance such that it operates in the inductive region. Moreover, the initial duty cycle is set to the minimum value to achieve a lower equivalent inverted voltage. This would result in soft-switching because the operation is in the inductive region. Moreover, because of the high frequency, the current gain would be low as explained in section 2.2.4. After this initial period, the voltage should be gradually increased back to its maximum value. This is done by decreasing the operating frequency to its nominal value, and then by increasing the duty cycle to 50% using phase-shift control. The proposed concept for the WPT start-up is shown qualitatively in Figure 3.18.

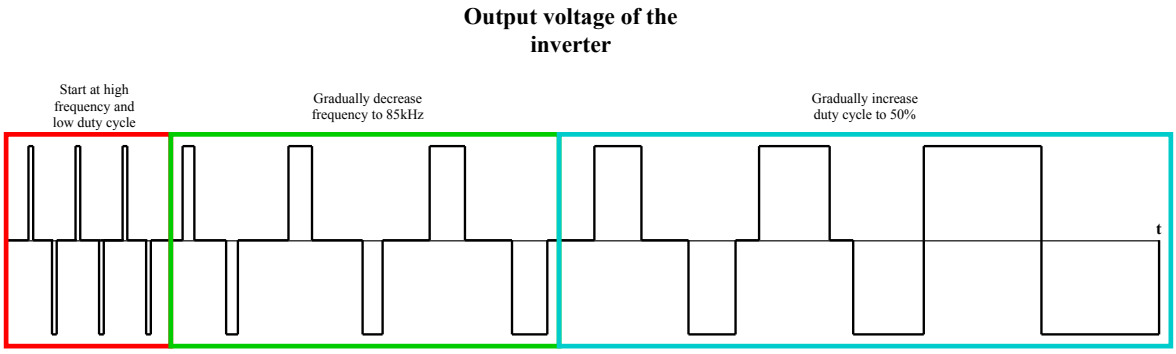

Figure 3.18: The concept of the start-up.

3.4.1. Simulation of the start-up

Circuit simulations of the start-up transient are done on a 1.1kW WPT system for both double-sided LCC and series-series compensation from Chapter 3.1. The simulations of the soft start-up are done in LTspice to show the performance of the WPT system. Different soft start-up methods are simulated in this section. These are based on Figure 3.18, and they use both the symmetrical and the asymmetrical phase-shift control.

Figure 3.19 shows the output voltage and current of the inverter simulated for the first 0.35ms when the soft start-up is not used. It is observed that, for the double-sided LCC compensation in Figure 3.19(a), the peak current almost reaches -25A when the soft start-up is not used which is about 5 times higher than the nominal current peak. The large peak currents at start-up would eventually result in tripping the over current protection which is also why it is important to have a soft start-up. Furthermore, soft-switching is lost for a few cycles. On the other hand, Figure 3.19(b) shows the output voltage and current of the inverter at the start for the series-series compensation. The starting current is much closer to the steady state value. However, soft switching is also lost for a few cycles just as for the double-sided LCC compensation.

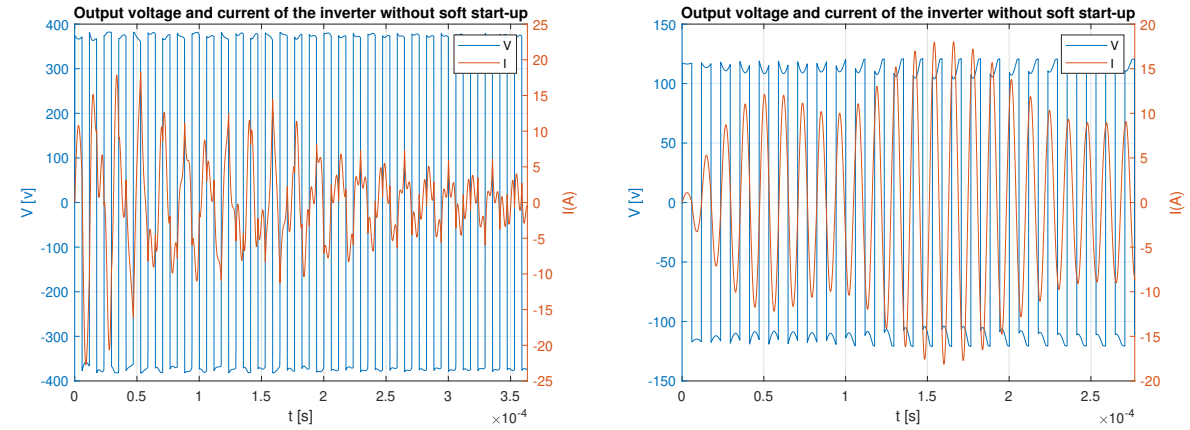

(a) (b)

Figure 3.19: The output voltage and current of the inverter without soft start-up for: (a) double-sided LCC compensation and (b) series-series compensation, frequency = 85kHz.

To avoid the high current peaks that might occur during the start-up transient, the influence of the soft start-up shown in Figure 3.18 has been analyzed on both the double-sided LCC and the series-series compensation networks. A challenge arises if the frequency is gradually decreased from 200kHz to 85kHz for the double-sided LCC. In Figure 3.20, the frequency gradually drops from 200kHz to 85kHz between 0-2ms. Then, until 6ms the duty cycle gradually increases from 5% to 50%. A peak current appears when the frequency reaches approximately 107kHz. The reason why these current peaks appear is due to the multiple resonances of the LCC. Moreover, it needs to be taken into account that these peaks can happen at other frequencies depending on the components' value that might vary because of their tolerances. However, the high starting frequency will result in soft switching after the first cycle.

One possible way to solve this problem is by using the soft start-up shown in Figure 3.21(a). First, the frequency will gradually decrease from 200kHz to 130kHz until 1ms. Afterward, it will go to 88kHz and decrease gradually to 85kHz until 2ms. Finally, the duty cycle will gradually increase back from 5% to 50%. Figure 3.21(b) shows that there will be soft-switching at the transition between 130kHz and 88kHz after a few cycles.

Another possible soft start-up strategy for the double-sided LCC could be using the symmetrical phase-shift without varying the operating frequency. This method is able to comply with the frequency limit 81.38-90kHz from the current standards. It is observed that there is a current peak at the start-up which is larger than the case where the frequency is changed, but the frequency would be in the range allowed by the standards. The duty cycle gradually increases from 5% to 50% between 0-3ms. Figure 3.22(b) show that there will be soft-switching at the start after almost 0.2ms.

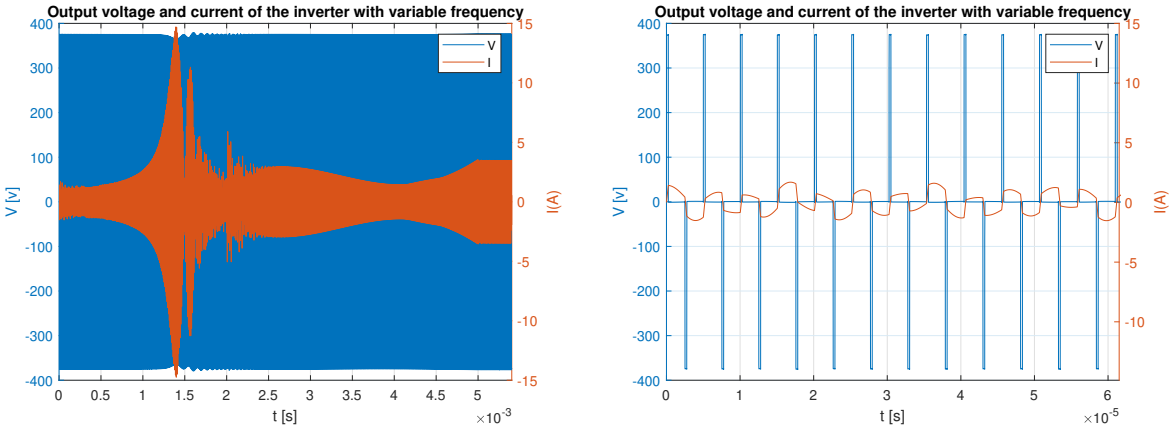

(a) (b)

Figure 3.20: The output voltage and current of the inverter with double-sided LCC compensation for a varying frequency between 0 and 2ms (a) full version and (b) zoomed-in version, resonance frequency = 85kHz.

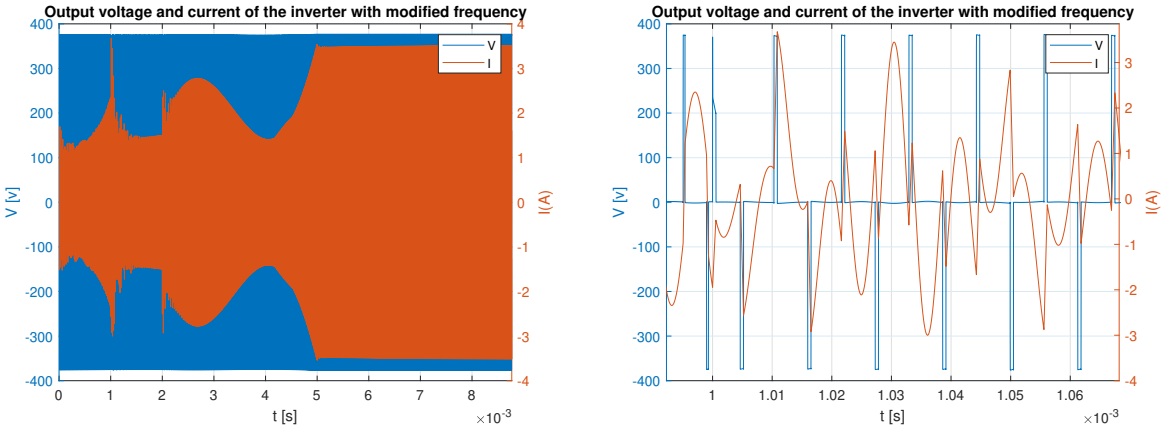

(a) (b)

Figure 3.21: The output voltage and current of the inverter for a double-sided LCC compensation with the frequency going from 130kHz to 88kHz at 1ms (a) full version and (b) zoomed-in version, resonance frequency = 85kHz.

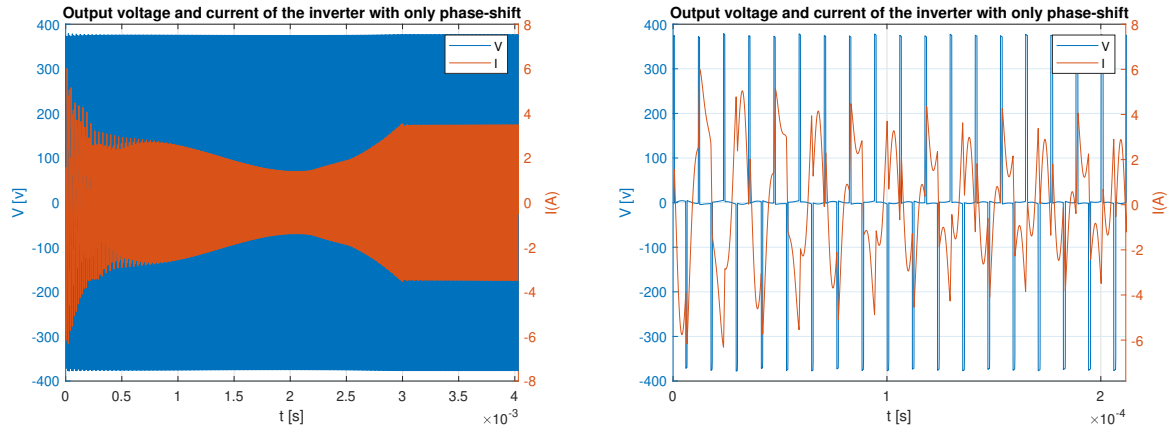

(a) (b)

Figure 3.22: The output voltage and current of the inverter for a double-sided LCC compensation with only symmetrical phase-shift (a) full version and (b) zoomed-in version, resonance frequency = 85kHz.

A similar analysis has been executed with the series-series compensation network. The symmetrical phase-shift control is used in Figure 3.23. It is shown that the starting current is much lower if compared with Figure 3.23(b). However, hard switching is introduced while it is using the symmetrical phase-shift. This might be resolved at a higher frequency because of the more inductive behavior.

Figure 3.24(a) shows the variable frequency and symmetrical phase-shift control with the series-series compensation network. Notably, the current starts at an even lower than the one with only symmetrical phase-shift control. Moreover, soft switching is observed at 200kHz from Figure 3.24(b), but hard switching will eventually happen at around 105kHz.

Lastly the asymmetrical phase-shift control is simulated in Figure 3.25(a) for the series-series compensation network. The starting current is much higher than the previous methods which makes sense if it is considered that only the positive pulse width is smaller. From 3.25(b) it can be seen that that there will eventually be hard switching. It might be possible to maintain soft-switching if a higher starting frequency is used. This is later investigated in Chapter 3.4.3.

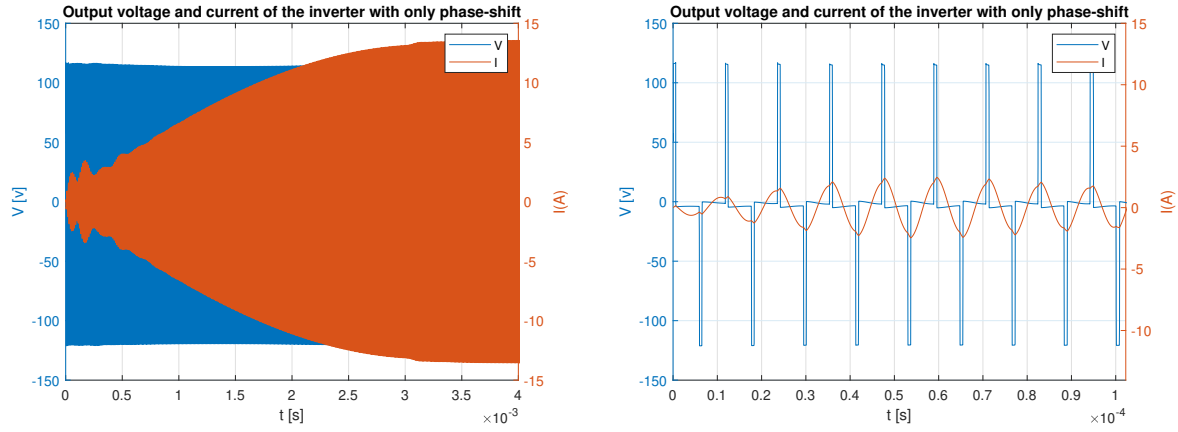

(a) (b)

Figure 3.23: The output current of the inverter with only symmetrical phase-shift for series-series compensation (a) full version and (b) zoomed-in version, resonance frequency = 85kHz.

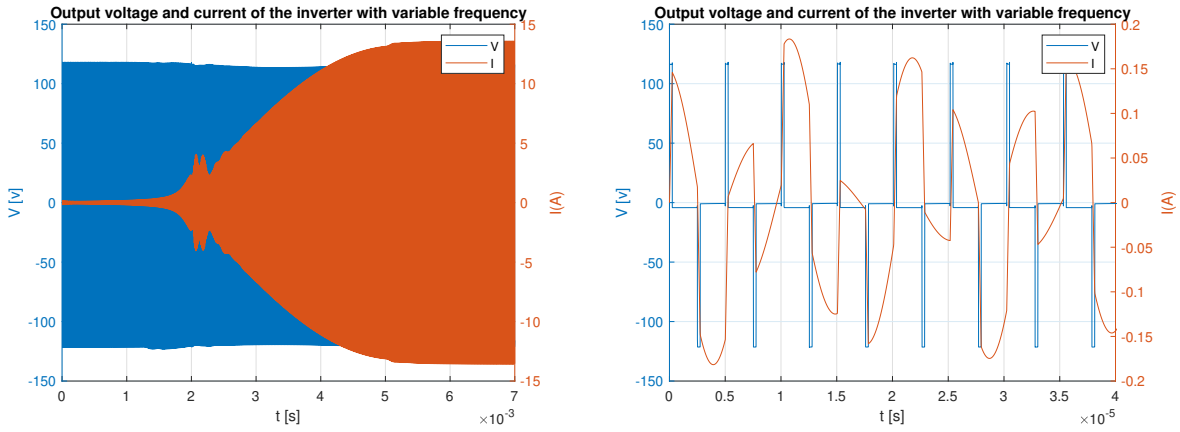

(a) (b)

Figure 3.24: The output current of the inverter with variable frequency and symmetrical phase-shift for series-series compensation (a) full version and (b) zoomed-in version, resonance frequency = 85kHz.

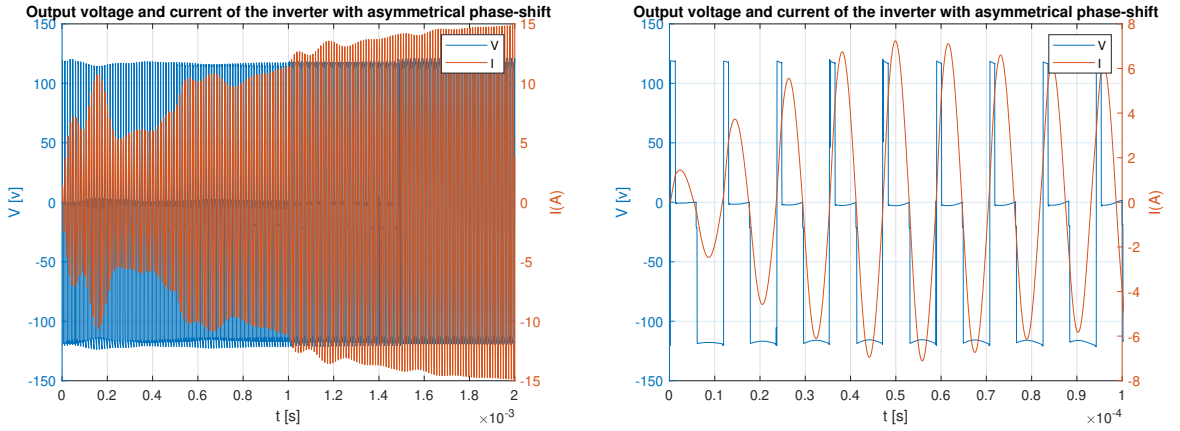

(a) (b)

Figure 3.25: The output current of the inverter with only asymmetrical phase-shift for series-series compensation (a) full version and (b) zoomed-in version, resonance frequency = 85kHz.

3.4.2. Programming of the start-up

The design of the controller is shown in Figure 3.27(a). The counter that is connected to the start-up is shown in Figure 3.27(b). It counts till it reaches the maximum count value and will stop at that value. The threshold of the switch should be set the same as the maximum count to achieve this. Each count is limited to 4ms. This means that the whole soft start-up process is done within 0.3s.

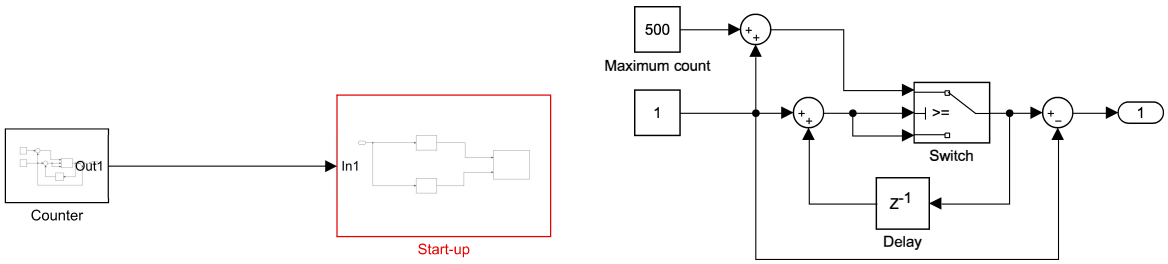

(a) (b)

Figure 3.26: (a) Main model and (b) counter subsystem.

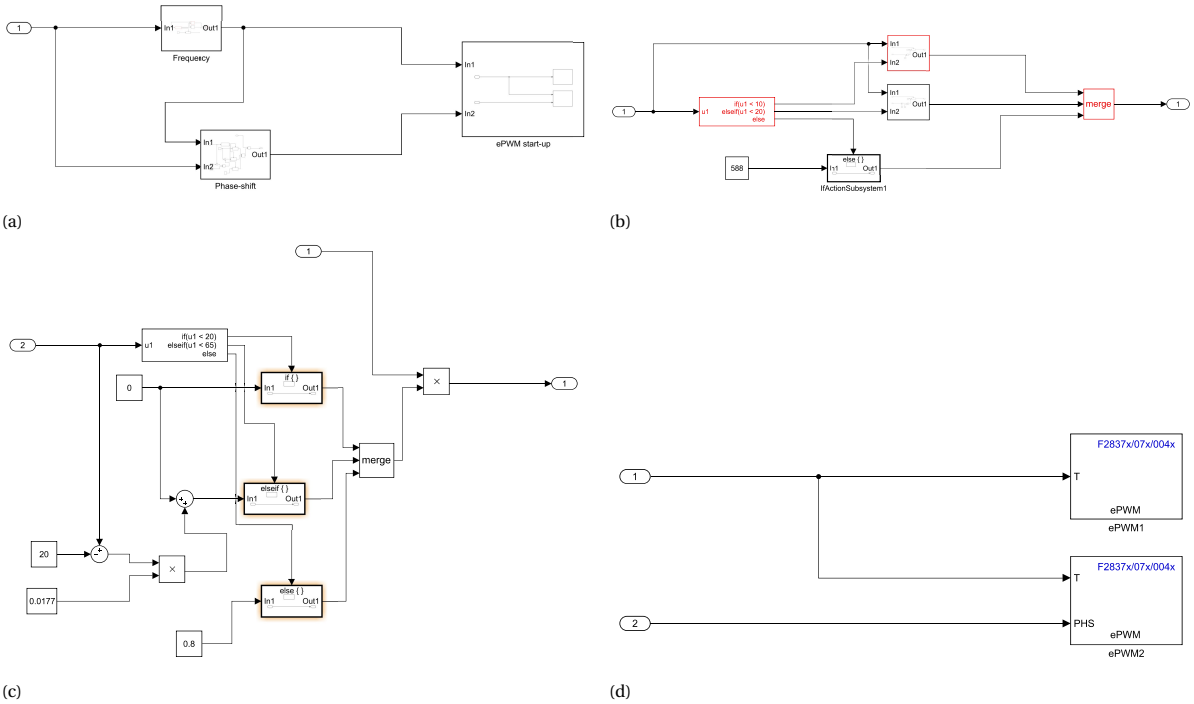

(a) (b) (c) (d)

Figure 3.27: Soft start-up: (a) overview for symmetrical phase-shift, (b) frequency control, (c) symmetrical phase-shift control and (d) PWM subsystem of the controller.

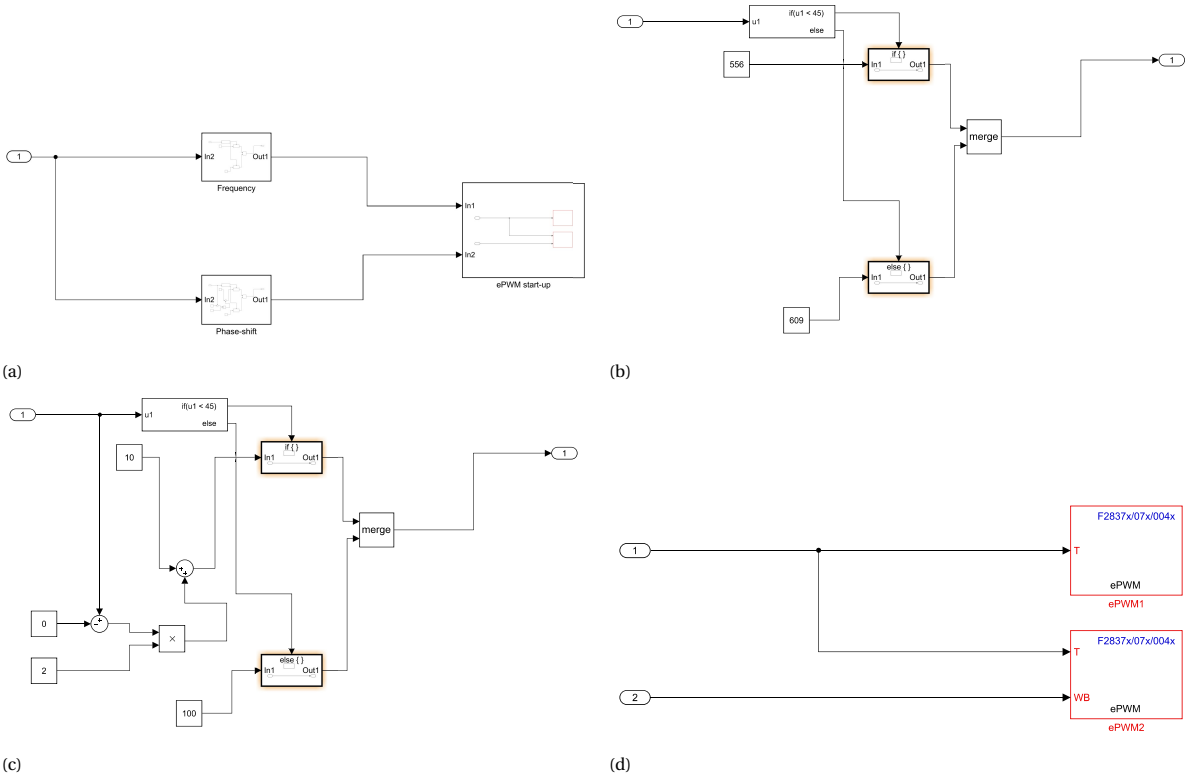

(a) (b) (c) (d)

Figure 3.28: Soft start-up: (a) overview, (b) frequency control, (c) asymmetrical phase-shift control and (d) PWM subsystem of the controller.

Figure 3.27(a) shows an overview of the symmetrical phase-shift control. The switching frequency is controlled by Figure 3.27(b). First, the frequency will gradually decrease from 200kHz to 130kHz. Then, it will go

from 88kHz to 85kHz. The timing when the frequencies change can be configured by changing the condition in the if-statement 3.27(b). Subsequently, the symmetrical phase-shift control is shown in Figure 3.27(c). It will keep the phase-shift in a certain way such that the duty cycle of the output voltage of the inverter is 5% until it reaches 85kHz. Afterward, it will gradually shift the phase difference between the PWM to increase the duty cycle of the output voltage of the inverter back to 50%. When the frequency would start at 200kHz, it is chosen to use 10% duty cycle instead of 5% to avoid issues due to the very small pulse width. Additionally, the deadband of the ePWM modules in Figure 3.27(d) are set from 400ns to 200ns.

The overview of the asymmetrical phase-shift control is shown in Figure 3.28(a). In Figure 3.28(b) the frequency control is presented. It allows the frequency to change when the soft start-up process is over by using the if-statement block. The asymmetrical phase-shift control is displayed in Figure 3.28(c). This system controls the duty cycle of the signals from ePWM2 as shown in Figure 3.28(d).

3.4.3. Testing of the soft start-up

The programmed control methods for the start-up are tested on the 1.1kW WPT system. These results will be compared with the simulations. Furthermore, it is chosen to test the double-sided LCC compensation at partial load with an input voltage of 150V and the series-series compensation with 47V. This is done because of safety reasons. Also, the resulting resonant frequency of the system turns out to be 82kHz instead of 85kHz for series-series compensation due to the manufacturing tolerances of the resonant components.

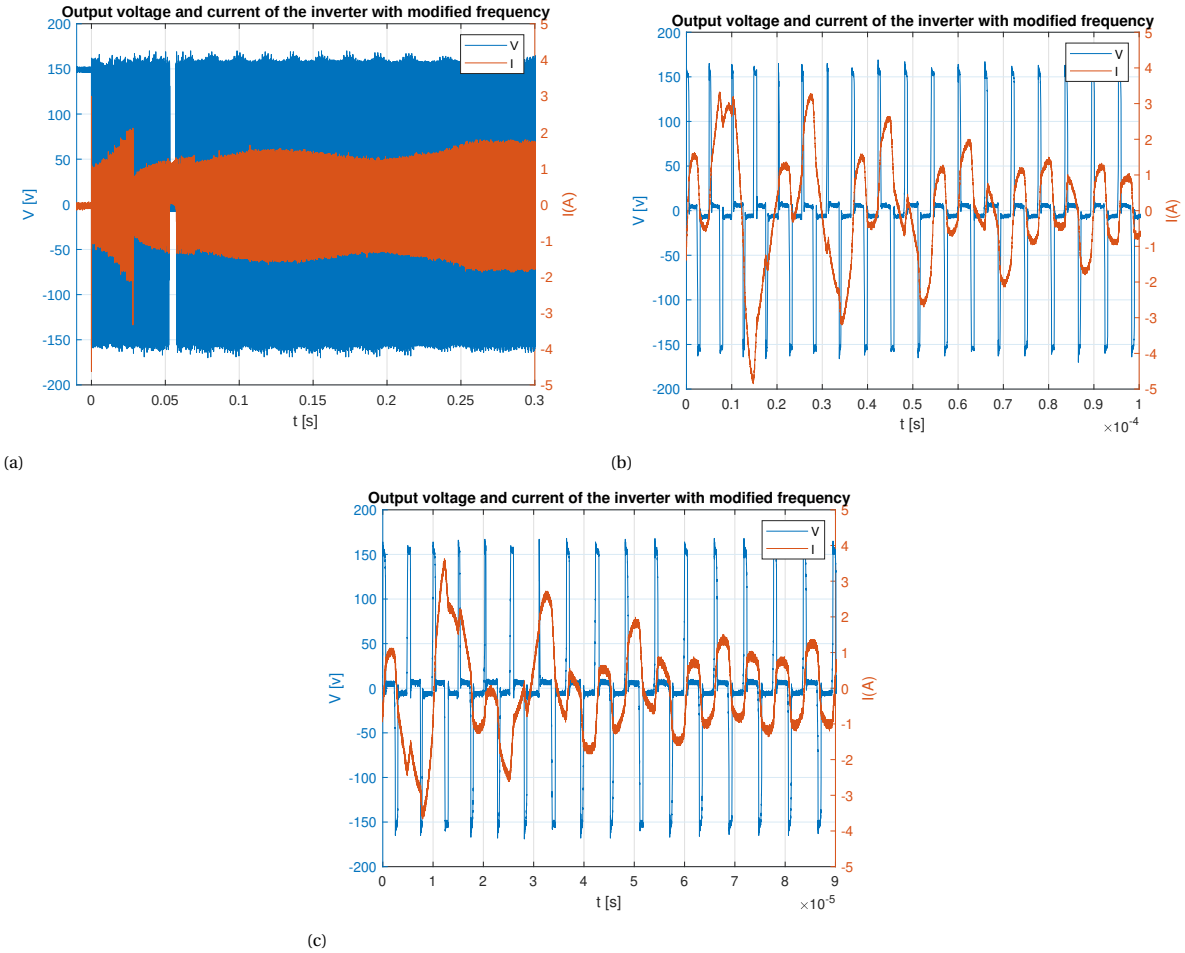

Figure 3.29: The output voltage and current of the inverter for the double sided LCC compensation with the frequency going from 130kHz to 88kHz at 1ms (a) full version, (b) zoomed-in version at the start and (c) zoomed-in version at the transition between 130kHz and 88kHz, resonance frequency = 85kHz and deadband = 200ns.

In Figure 3.29(a) the output voltage and current of the inverter are presented for double-sided LCC compensation with both frequency and symmetrical phase-shift control. The current waveform shows a similar

behavior as the simulation from Figure 3.21(a). It can be concluded that the peak current from Figure 3.29(b) would be even higher at full power because the simulation is done with an input voltage of 380V while this measurement is done with an input voltage of 150V. Besides, soft-switching is achieved at the start and when the frequency skips from 130kHz to 88kHz as shown in Figure 3.29(b) and 3.29(c).

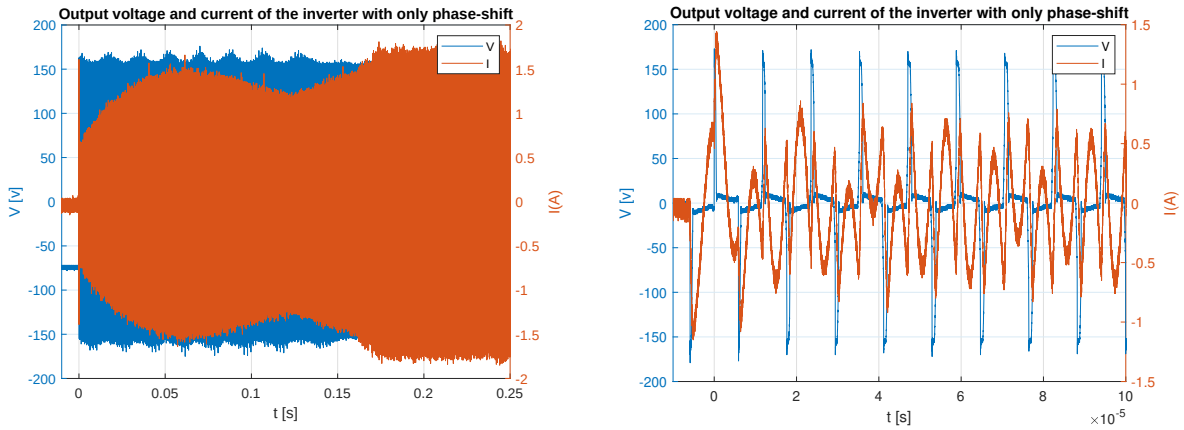

(a) (b)

Figure 3.30: The output voltage and current of the inverter for the double sided LCC compensation with only symmetrical phase-shift (a) full version and (b) zoomed-in version, resonance frequency = 85kHz and deadband = 400ns.

The output voltage and current for the symmetrical phase-shift control are shown in Figure 3.30(a) which is also tested on the double-sided LCC compensation network. The behavior of the current is also similar to the simulation from Figure 3.22(a). The starting current is much lower than shown in the simulation even though this is done on partial load. Moreover, soft-switching is secured after the first cycle as displayed in Figure 3.30(b). So, it seems that this method is better suited for double-sided LCC compensation than using both frequency and symmetrical phase-shift control.

The voltage and current behavior that is shown in Figure 3.31(a) is also similar to the simulation for the series-series compensation network. It can be seen from Figure 3.31(b) that there is hard-switching just as in the simulation. If variable frequency control is included it will result in Figure 3.32(a). It is demonstrated in Figure 3.32(b) that there will be soft-switching at the start, but when the frequency comes closer to the nominal frequency it would be lost. Next, the asymmetrical phase-shift is tested in Figure 3.33(a). It is noted that the current at the start is higher because the negative voltage pulse width stays constant. Here soft-switching is also lost as shown in Figure 3.33(b).

It is interesting to see if a higher frequency at the start could help to achieve soft-switching if the series-series compensation network is used. This is done for the symmetrical phase-shift in Figure 3.34(a). It can be observed from Figure 3.34(b) that there will barely be soft-switching after a few cycles. A similar strategy has been executed for the asymmetrical phase-shift in Figure 3.35(a) as it also starts at 89kHz. Figure 3.35(b) shows that there will be soft-switching after the first cycle. So, it seems that the asymmetrical phase-shift would be better to use for series-series compensation if started at a higher frequency.

It can be concluded that the experimental results from the soft start-up investigation have similar behaviour as the simulated ones in Chapter 3.4.1 It must to be pointed out that the amplitude of the current waveform from the inverter is lower in the measurements because the applied input voltage is lower. Moreover, the results can be summarized as follows:

- The double-sided LCC compensation is found to perform the best with using only the symmetrical phase-shift control. It provides soft-switching after the first cycle and it has a lower peak current than using symmetrical phase-shift control with frequency control.
- The series-series compensation achieves the best result with the asymmetrical phase-shift control when started at 89kHz. It produces a relatively low starting current and provides soft-switching after the first cycle.

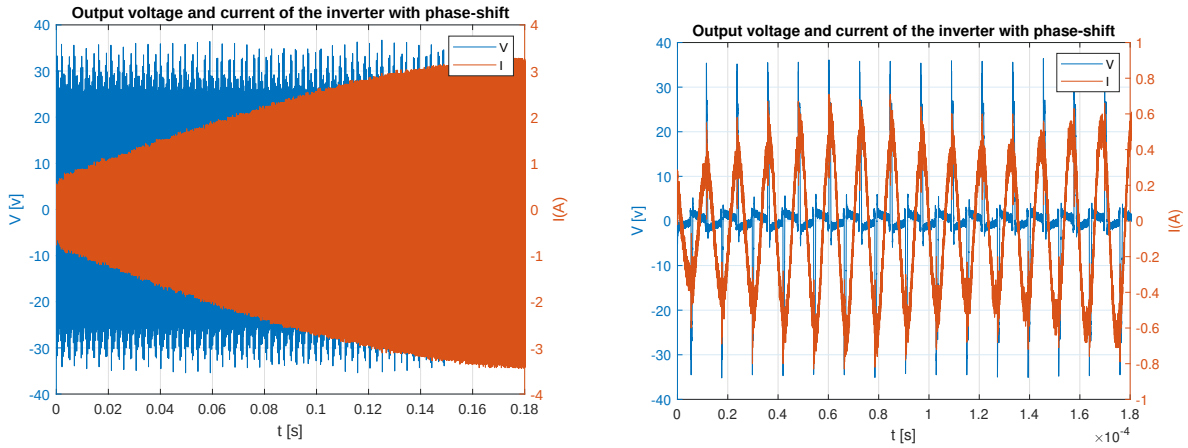

(a) (b)

Figure 3.31: The output voltage and current of the inverter of the series-series compensation with only symmetrical phase-shift (a) full version and (b) zoomed-in version, resonance frequency = 82kHz and deadband = 400ns.

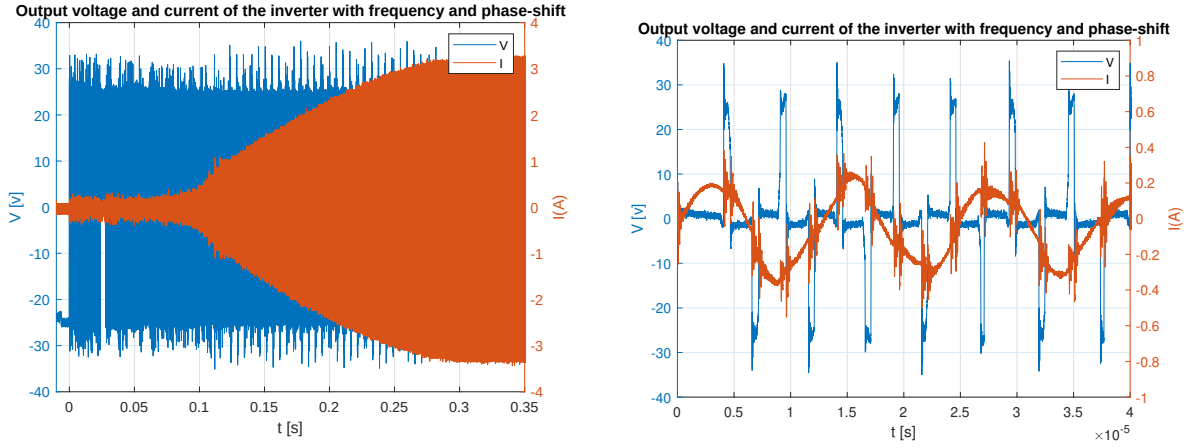

(a) (b)

Figure 3.32: The output voltage and current of the inverter of the series-series compensation with variable frequency and symmetrical phase-shift (a) full version and (b) zoomed-in version, resonance frequency = 82kHz and deadband = 200ns.

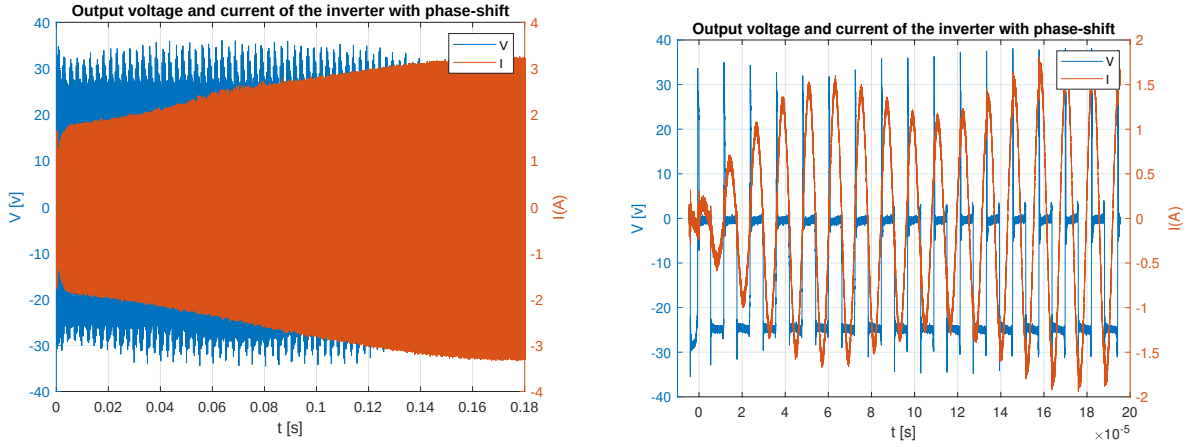

(a) (b)

Figure 3.33: The output voltage and current of the inverter of the series-series compensation with asymmetrical phase-shift (a) full version and (b) zoomed-in version, resonance frequency = 82kHz and deadband = 400ns.

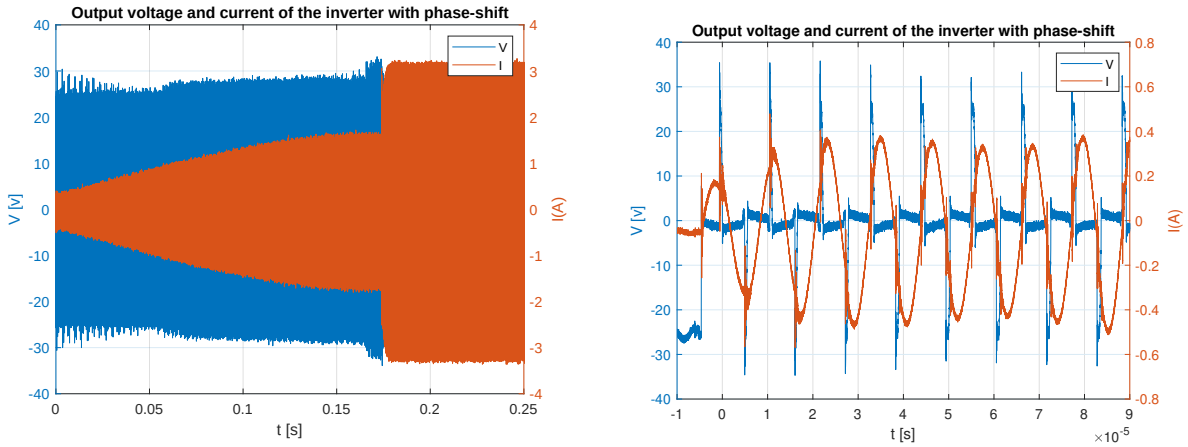

(a) (b)

Figure 3.34: The output voltage and current of the inverter of the series-series compensation with symmetrical phase-shift starting at 89kHz (a) full version and (b) zoomed-in version, resonance frequency = 82kHz and deadband = 400ns.

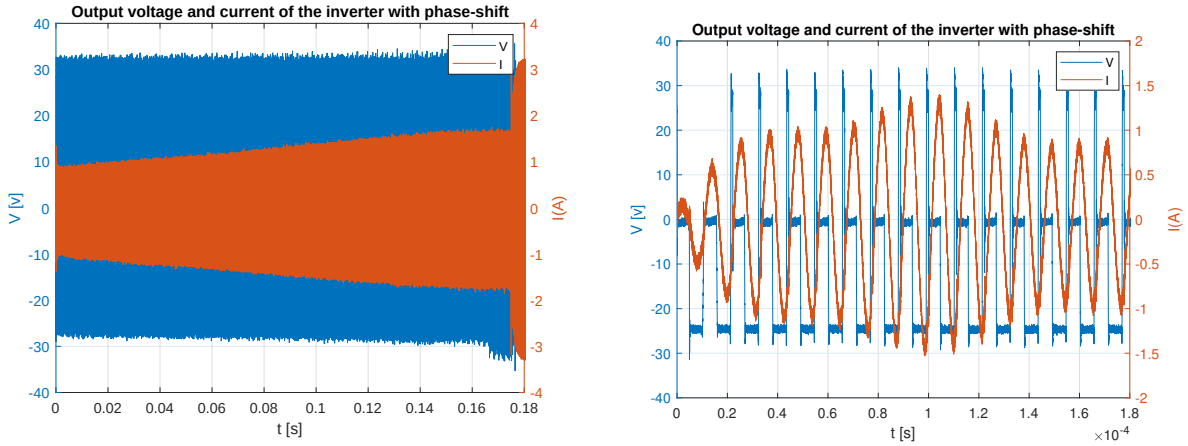

(a) (b)

Figure 3.35: The output voltage and current of the inverter of the series-series compensation with asymmetrical phase-shift starting at 89kHz (a) full version and (b) zoomed-in version, resonance frequency = 82kHz and deadband = 400ns.

3.4.4. Concept of the soft shut-down

When the battery is around 80% charged it will go from constant current mode to constant voltage mode. This will gradually increase the resistance of the load which will increase the voltage and current at the secondary side and the output current of the inverter. The increase of the voltage and current at the secondary side could potentially damage the converters at the secondary side. However, because the output current of the inverter also increases, the over-current protection would stop this from happening. On the other hand, if it is necessary to use the over-current protection to shut-down the system every time, it could overwork the protection which would decrease the durability of the whole system. Another shut-down method is shown in Figure 3.36. First, the soft shut-down gradually decreases the duty cycle of the output voltage of the inverter. Thereafter, it increases the frequency from 85kHz to 200kHz and lastly turns off the inverter voltage. In Appendix B is the simulation given and a concept on how to program this soft shut-down strategy.

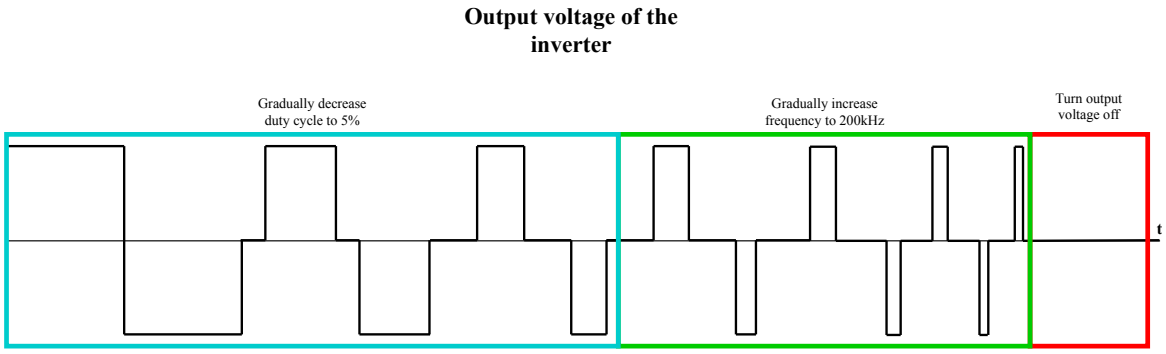

Figure 3.36: The concept of the soft shut-down.

4

Conclusion & Future Work

With the rise of EVs, it has become interesting to use wireless power transfer or WPT for this charging application. However, there are some challenges involved with this technology. This work aimed to understand the challenges that are involved with the feedback control implementation of a WPT system in a TI microcontroller which integrates an analog zero current detection circuit to ensure that soft-switching is attained for all operating conditions, and finally to include other functionalities such as soft start-up, soft shut-down, and over-current protection.

4.1. Conclusion

The literature research that is done in Chapter 2, helped to create an understanding of the challenges in the control of WPT systems. It is also a necessity to ensure soft-switching to comply with the efficiency requirements and magnetic field limits. To ensure soft-switching, the resonant converter is set to be operated in the inductive region. Hence, the switching frequency of the inverter is set to be slightly above the resonance frequency to also maximize efficiency which is shown in the analysis from Chapter 2.2.4. It also shows that this efficiency is also dependent on the coupling between the coils and the load resistance. It is preferable to operate at the optimum load that minimizes the losses of the coils and that depends on the mutual inductance of the coils, the resonance frequency and the resistance of the coils. It is desirable to ensure a coupling between the coils that is as high as possible. Moreover, the current standards limit the switching frequency to 81.38-90kHz which means that the control is required to be fast and of high bandwidth. This is why a combination of analog and digital control is used. The analog control has a fast response while the digital control is able to do complex tasks.

The start of the digital control began after the literature research. The open-loop control is realized to gain experience on the TI F28379D Launchpad. Herein, the implemented program is able to vary the switching frequency and dead time via a serial communication. Afterward, the closed-loop control is designed which works together with an analog circuit which detects a zero-crossing in the output current of the inverter. Typically the digital control would slow the control down, however the tripzone submodule of the F28379D Launchpad would negate this because of it's fast response. The closed-loop control is tested with the analog control and is able to produce the desired PWM from a test signal with a dead time that can be changed via serial communication.

Likewise, the over-current protection is implemented with closed-loop control. It works together with some analog control similar to the closed-loop control. The results show that it works and reacts in about 66ns. This speed is well suitable to safeguard to operation and reliability of the WPT system.

The soft start-up shows that it is better to use only symmetrical phase-shift control for the double-sided LCC compensation. Unlike the simulations, it results in a low starting peak current and after the first cycle, it achieves soft-switching. Besides, it also complies with the current standards. Asymmetrical phase-shift control when started at a higher frequency seems to be the best control strategy for series-series compensation. It produces a lower current at the start and accomplishes soft-switching after the first cycle. For the soft

shut-down a concept is made which works with a similar control strategy as the soft start-up.

4.2. Future Work

Now that most of the project is finished, it is unavoidable to set some plans for some future work and recommendations. These plans are:

- It should be investigated what is the influence for using a battery as a load instead of a resistor.
- Soft shut-down needs more investigation.
- Closed-loop control need to be tested with high power.
- All the features need to be integrated with the closed-loop control.
- A method for frequency limitation is needed for the closed-loop control to agree with the requirements of the current standards.
- Some further research needs to be done on different communication methods.

A

Additional C-code

A.1. Enable action qualifier with trip zone

```
EALLOW;
EPwm1Regs.AQTSRCSEL.bit.T1SEL = 0b0000; /* Select TZ1 as an event source */
EPwm1Regs.AQCTLA2.bit.T1U = 0b11; /* Action when event occurs on T1 in UP-Count, 11: Set: toggle ePWM1A output. */
EPwm1Regs.AQCTLA2.bit.T1D = 0b11; /* Action when event occurs on T1 in Down-Count, 11: Set: toggle ePWM1A output. */

EPwm1Regs.AQCTLB2.bit.T1U = 0b11; /* Action when event occurs on T1 in UP-Count, 11: Set: toggle ePWM1B output. */
EPwm1Regs.AQCTLB2.bit.T1D = 0b11; /* Action when event occurs on T1 in Down-Count, 11: Set: toggle ePWM1B output. */

EPwm2Regs.AQTSRCSEL.bit.T1SEL = 0b0000; /* Select TZ1 as an event source */

EPwm2Regs.AQCTLA2.bit.T1U = 0b11; /* Action when event occurs on T1 in UP-Count, 11: Set: toggle ePWM2A output. */
EPwm2Regs.AQCTLA2.bit.T1D = 0b11; /* Action when event occurs on T1 in Down-Count, 11: Set: toggle ePWM2A output. */

EPwm2Regs.AQCTLB2.bit.T1U = 0b11; /* Action when event occurs on T1 in UP-Count, 11: Set: toggle ePWM2B output. */
EPwm2Regs.AQCTLB2.bit.T1D = 0b11; /* Action when event occurs on T1 in Down-Count, 11: Set: toggle ePWM2B output. */

EPwm5Regs.AQTSRCSEL.bit.T1SEL = 0b0000; /* Select TZ1 as an event source*/

EPwm5Regs.AQCTLA2.bit.T1U = 0b01; /* Action when event occurs on T1 in UP-Count, 11: Set: low ePWM5A output. */
EPwm5Regs.AQCTLA2.bit.T1D = 0b01; /* Action when event occurs on T1 in Down-Count, 11: Set: low ePWM5A output. */

EDIS;
```

B

Simulation and programming of the soft shut-down

Simulations on the shut-down are done in LTspice to present what happens if there is no soft shut-down, with duty cycle decreasing from 50% to 5%, with the method shown in Figure 3.36 and with a jump in frequency similar to the final soft start-up concept. This is done on the circuit of Figure B.1 with the parameters given in Table B.1. In the simulation the resistance of the load increases over time this is a simplified scenario that is used to mimic the behavior of the battery.

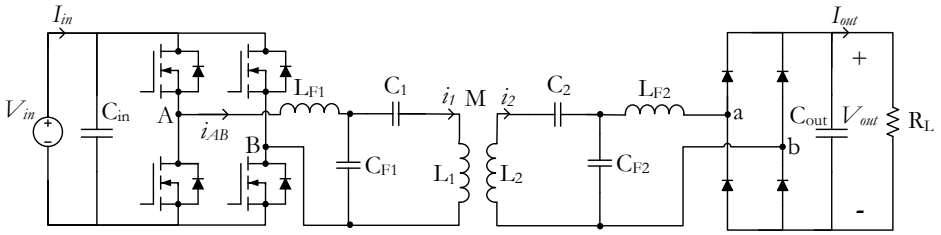

Figure B.1: Double-sided LCC compensation network.

Table B.1: Component values of the 7.7kW EV charger.

Parameter	Value [unit]
L_1	63.3489 [μH]
L_2	43.533 [μH]
L_{F1}	23.54 [μH]
L_{F2}	14.49 [μH]
C_1	88.07 [nF]
C_2	120.7 [nF]
C_{F1}	148.93 [nF]
C_{F2}	242.02 [nF]

Figure B.2 shows the plot of the secondary current. It can be observed that the current in the coil would increase gradually as the load resistance increases. As a consequence, the relatively high current could damage the equipment of the system. On the contrary, with the soft shut-down, the current would eventually go to zero.

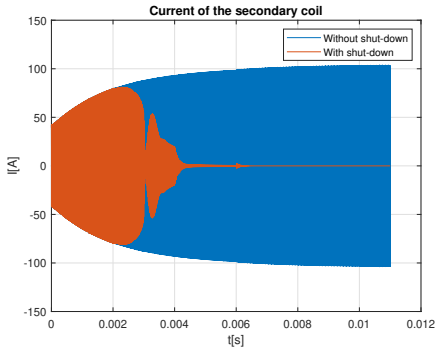

Figure B.2: Current through the secondary coil with and without shut-down.

In Figure B.3, the duty cycle decreases from 50% to 5% between 0-3ms. Then, the output voltage of the inverter is turned off. It is observed that the current gradually lowers when it gets near the 3ms mark. So, this looks like a promising method.

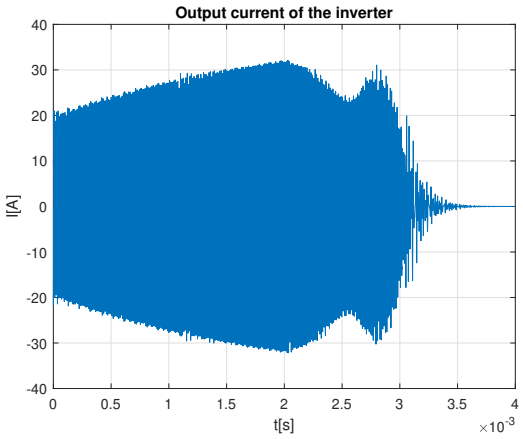

Figure B.3: Output current of the inverter with only lowering the duty cycle.

In Figure B.4, the duty cycle decreases gradually from 50% to 5% between 0-3ms. Afterward, the frequency of the output current of the inverter gradually increases from 85kHz to 200kHz between 3-16ms. A similar effect happens at approximately 107kHz as in the start-up and the peak can vary between 100-115kHz depending on the component values. This peak current also exists because of the multiple resonances just as for the start-up. Similarly to the previous analysis, a primary components' tolerance of 5% is used while the secondary side's tolerances are neglected because of the minimal effect on the resonance. Furthermore, it shows that the current is lower at higher frequencies, which implies that there is a lower current gain at higher frequencies. Besides, it will also ensure soft-switching of the inverter as it is in the inductive region.

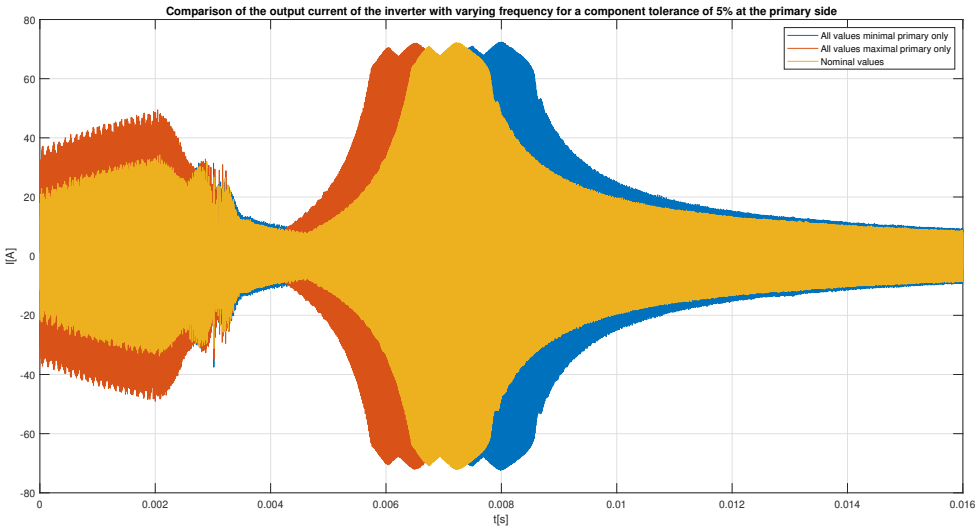

Figure B.4: Comparison of the output current of the inverter for a varying frequency between 3ms and 16ms for a component tolerance of 5%.

The last simulated method for the soft shut-down is to first decrease the duty cycle of the output voltage gradually to 5%. Subsequently, the frequency will first gradually go to 90kHz and then jump similarly to the start-up to 150kHZ. Afterward, the frequency will gradually increase to 200kHZ. Lastly, the duty cycle will drop to 0% which will turn the system off. However, it shows a less steady drop of the current in comparison to only decreasing the duty cycle. So, it is finally decided to use that method

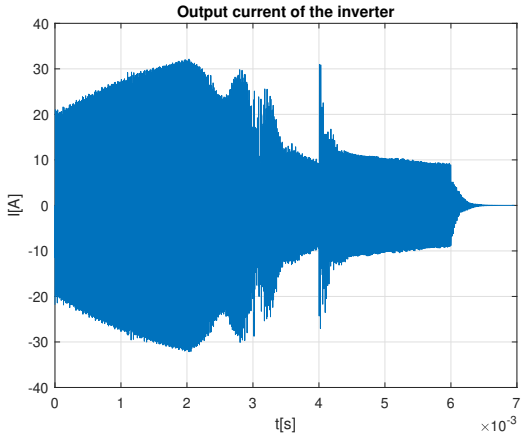

Figure B.5: Output current of the inverter with lowering the duty cycle gradually and increasing the frequency gradually.

The shut-down has a similar design to the start-up as shown in Figure B.6(a). The design of the counter in Figure B.6(b) is a modified version of the one in the start-up. The counter will only start counting if one of the pins on Launchpad goes from a low signal to a high signal.

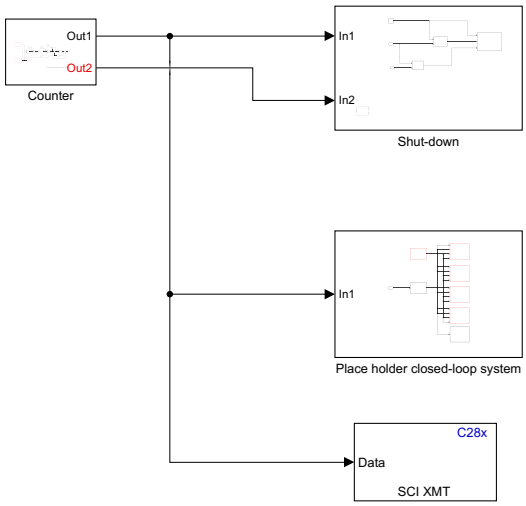

(a)

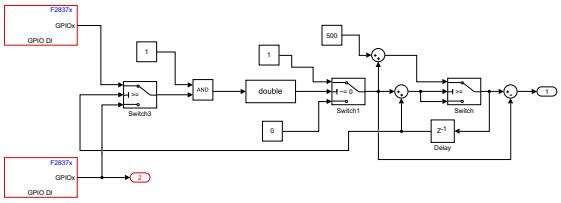

(b)

Figure B.6: Overview of the shut-down (a) and counter subsystem (b).

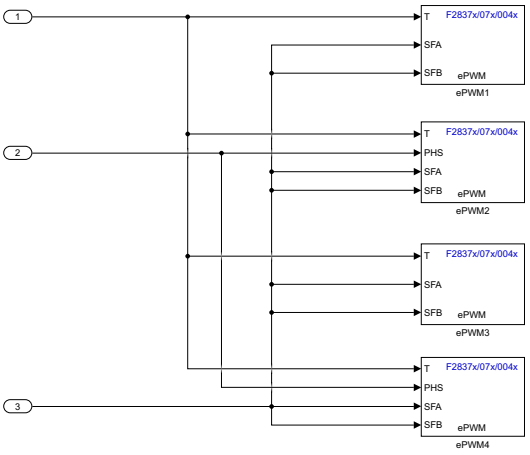

(a)

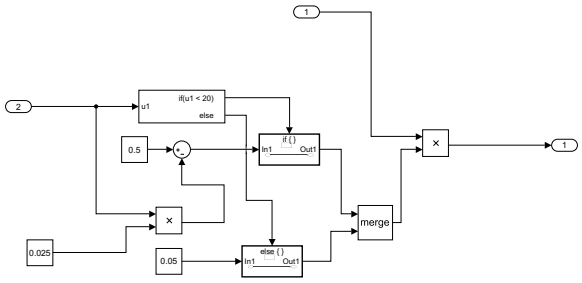

(b)

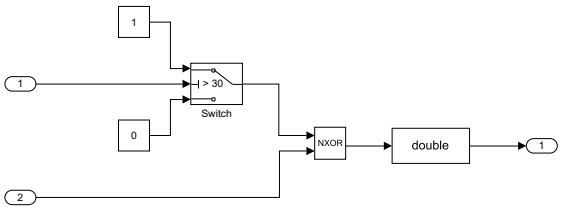

(c)

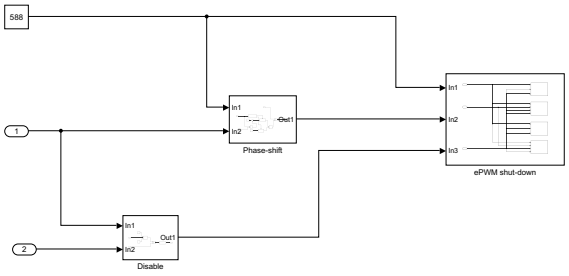

(d)

Figure B.7: PWM subsystem (a), Phase-shift control subsystem (b), disable (c) and PWM (d) of the start-up controller.

Figure B.7(a) shows the PWM control of the shut-down which is similar to the one of the soft start-up. The duty cycle control in Figure B.7(b) gradually decreases the duty cycle of the output voltage of the inverter. The disable in Figure B.7(c) makes sure that the shut-down is off when there is no signal that it needs it or when the counter reaches a certain value.

Bibliography

[1] P. Si, A. P. Hu, S. Malpas, and D. Budgett, "A frequency control method for regulating wireless power to implantable devices," *IEEE Transactions on Biomedical Circuits and Systems*, vol. 2, no. 1, pp. 22–29, March 2008.

[2] Chang-Gyun Kim, Dong-Hyun Seo, Jung-Sik You, Jong-Hu Park, and B. H. Cho, "Design of a contactless battery charger for cellular phone," *IEEE Transactions on Industrial Electronics*, vol. 48, no. 6, pp. 1238–1247, Dec 2001.

[3] T. Deyle and M. Reynolds, "Surface based wireless power transmission and bidirectional communication for autonomous robot swarms," in *2008 IEEE International Conference on Robotics and Automation*, May 2008, pp. 1036–1041.

[4] D. Patil, M. K. McDonough, J. M. Miller, B. Fahimi, and P. T. Balsara, "Wireless power transfer for vehicular applications: Overview and challenges," *IEEE Transactions on Transportation Electrification*, vol. 4, no. 1, pp. 3–37, March 2018.

[5] W. Zhang and C. C. Mi, "Compensation topologies of high-power wireless power transfer systems," *IEEE Transactions on Vehicular Technology*, vol. 65, no. 6, pp. 4768–4778, June 2016.

[6] H. H. Wu, A. Gilchrist, K. D. Sealy, and D. Bronson, "A high efficiency 5 kw inductive charger for evs using dual side control," *IEEE Transactions on Industrial Informatics*, vol. 8, no. 3, pp. 585–595, Aug 2012.

[7] ISO/PAS19363:2017, "Electrically propelled road vehicles - magnetic field wireless power transfer - Safety and interoperability requirements," ISO, Standard, Jan. 2017.

[8] N. Mohan, T. Undeland, and W. Robbins, *Power Electronics Converters, Application and Design Second Edition*. New York: John Wiley & Sons, 1995.

[9] *Power Factor Correction (PFC) Handbook*, ON Semiconductor, April 2014, rev. 5.

[10] *PFC boost converter design guide*, Infineon, February 2016, rev. 1.1.

[11] F. Grazian, P. van Duijsen, T. B. Soeiro, and P. Bauer, "Advantages and tuning of zero voltage switching in a wireless power transfer system," in *2019 IEEE PELS Workshop on Emerging Technologies: Wireless Power Transfer (WoW)*, June 2019, pp. 367–372.

[12] S. Chopra and P. Bauer, "Analysis and design considerations for a contactless power transfer system," in *2011 IEEE 33rd International Telecommunications Energy Conference (INTELEC)*, Oct 2011, pp. 1–6.

[13] S. Li, W. Li, J. Deng, T. D. Nguyen, and C. C. Mi, "A double-sided LCC compensation network and its tuning method for wireless power transfer," *IEEE Transactions on Vehicular Technology*, vol. 64, no. 6, pp. 2261–2273, June 2015.

[14] R. C. Fernandes and A. A. de Oliveira, "Theoretical bifurcation boundaries for wireless power transfer converters," in *2015 IEEE 13th Brazilian Power Electronics Conference and 1st Southern Power Electronics Conference (COBEP/SPEC)*, Nov 2015, pp. 1–4.

[15] Chwei-Sen Wang, G. A. Covic, and O. H. Stielau, "General stability criterions for zero phase angle controlled loosely coupled inductive power transfer systems," in *IECON'01. 27th Annual Conference of the IEEE Industrial Electronics Society (Cat. No.37243)*, vol. 2, Nov 2001, pp. 1049–1054 vol.2.

[16] R. L. Steigerwald, "A comparison of half-bridge resonant converter topologies," *IEEE Transactions on Power Electronics*, vol. 3, no. 2, pp. 174–182, April 1988.

[17] F. Ulaby and U. Ravaioli, *Fundamentals of Applied Electromagnetics Seventh Edition Global Edition*. Harlow England: Pearson, 2015.

[18] M. Budhia, J. T. Boys, G. A. Covic, and C. Huang, "Development of a single-sided flux magnetic coupler for electric vehicle ipt charging systems," *IEEE Transactions on Industrial Electronics*, vol. 60, no. 1, pp. 318–328, Jan 2013.

[19] S. Bandyopadhyay, J. Dong, Z. Qin, and P. Bauer, "Comparison of optimized chargepads for wireless ev charging application," in *2019 10th International Conference on Power Electronics and ECCE Asia (ICPE 2019 - ECCE Asia)*, May 2019, pp. 1–8.

[20] D. Ongayo and M. Hanif, "Comparison of circular and rectangular coil transformer parameters for wireless power transfer based on finite element analysis," in *2015 IEEE 13th Brazilian Power Electronics Conference and 1st Southern Power Electronics Conference (COBEP/SPEC)*, Nov 2015, pp. 1–6.

[21] M. Budhia, G. Covic, and J. Boys, "A new ipt magnetic coupler for electric vehicle charging systems," in *IECON 2010 - 36th Annual Conference on IEEE Industrial Electronics Society*, Nov 2010, pp. 2487–2492.

[22] G. A. Covic, M. L. G. Kissin, D. Kacprzak, N. Clausen, and H. Hao, "A bipolar primary pad topology for ev stationary charging and highway power by inductive coupling," in *2011 IEEE Energy Conversion Congress and Exposition*, Sep. 2011, pp. 1832–1838.

[23] A. Zaheer, G. A. Covic, and D. Kacprzak, "A bipolar pad in a 10-khz 300-w distributed ipt system for agv applications," *IEEE Transactions on Industrial Electronics*, vol. 61, no. 7, pp. 3288–3301, July 2014.

[24] IEC61980-1, "Electric vehicle wireless power transfer (WPT) systems - part 1: General requirements," IEC, Standard, Jul. 2015.

[25] International Commission on Non-Ionizing Radiation Protection, "ICNIRP guidelines for limiting exposure to time-varying electric and magnetic fields (1Hz–100kHz)," ICNIRP, Standard, 2010.

[26] J2954RP, "Wireless power transfer for Light-Duty Plug-In/ Electric Vehicles and Alignment Methodology," SAE International, Standard, Apr. 2019.

[27] F. Grazian, W. Shi, J. Dong, P. van Duijsen, T. B. Soeiro, and P. Bauer, "Survey on standards and regulations for wireless charging of electric vehicles," in *2019 AEIT International Conference of Electrical and Electronic Technologies for Automotive (AEIT AUTOMOTIVE)*, July 2019, pp. 1–5.

[28] R. Bosshard, U. Badstübner, J. W. Kolar, and I. Stevanović, "Comparative evaluation of control methods for inductive power transfer," in *2012 International Conference on Renewable Energy Research and Applications (ICRERA)*, Nov 2012, pp. 1–6.

[29] J. Zhang, J. Zhao, Y. Zhang, and F. Deng, "A wireless power transfer system with dual switch-controlled capacitors for efficiency optimization," *IEEE Transactions on Power Electronics*, vol. 35, no. 6, pp. 6091–6101, 2020.

[30] J. M. Burdio, L. A. Barragan, F. Monterde, D. Navarro, and J. Acero, "Asymmetrical voltage-cancellation control for full-bridge series resonant inverters," *IEEE Transactions on Power Electronics*, vol. 19, no. 2, pp. 461–469, 2004.

[31] C. Huang, J. T. Boys, and G. A. Covic, "Lcl pickup circulating current controller for inductive power transfer systems," *IEEE Transactions on Power Electronics*, vol. 28, no. 4, pp. 2081–2093, April 2013.

[32] Chwei-Sen Wang, G. A. Covic, and O. H. Stielau, "Power transfer capability and bifurcation phenomena of loosely coupled inductive power transfer systems," *IEEE Transactions on Industrial Electronics*, vol. 51, no. 1, pp. 148–157, Feb 2004.

[33] R. Bosshard, J. W. Kolar, and B. Wunsch, "Control method for inductive power transfer with high partial-load efficiency and resonance tracking," in *2014 International Power Electronics Conference (IPEC-Hiroshima 2014 - ECCE ASIA)*, May 2014, pp. 2167–2174.

[34] T. Diekhans and R. W. De Doncker, "A dual-side controlled inductive power transfer system optimized for large coupling factor variations and partial load," *IEEE Transactions on Power Electronics*, vol. 30, no. 11, pp. 6320–6328, Nov 2015.

[35] K. Hata, T. Imura, and Y. Hori, "Maximum efficiency control of wireless power transfer via magnetic resonant coupling considering dynamics of dc-dc converter for moving electric vehicles," in *2015 IEEE Applied Power Electronics Conference and Exposition (APEC)*, March 2015, pp. 3301–3306.

[36] H. Ishihara, F. Moritsuka, H. Kudo, S. Obayashi, T. Itakura, A. Matsushita, H. Mochikawa, and S. Otaka, "A voltage ratio-based efficiency control method for 3 kw wireless power transmission," in *2014 IEEE Applied Power Electronics Conference and Exposition - APEC 2014*, March 2014, pp. 1312–1316.

[37] F. Grazian, "Control of a resonant wireless e-bike charging converter," Master's thesis, Delft University of Technology, 2018.

[38] S. Liu, Y. Shen, Y. Wu, J. Lin, and M. Hu, "Study on frequency tracking for wireless power transfer system using magnetic resonant coupling," in *2018 13th IEEE Conference on Industrial Electronics and Applications (ICIEA)*, May 2018, pp. 2569–2572.

[39] H. L. Li, A. P. Hu, and G. A. Covic, "Fpga controlled high frequency resonant converter for contactless power transfer," in *2008 IEEE Power Electronics Specialists Conference*, June 2008, pp. 3642–3647.

[40] N. Y. Kim, K. Y. Kim, Y. Ryu, J. Choi, D. Kim, C. Yoon, Y. Park, and S. Kwon, "Automated adaptive frequency tracking system for efficient mid-range wireless power transfer via magnetic resonanc coupling," in *2012 42nd European Microwave Conference*, Oct 2012, pp. 221–224.

[41] J. M. Miller, O. C. Onar, and M. Chinthavali, "Primary-side power flow control of wireless power transfer for electric vehicle charging," *IEEE Journal of Emerging and Selected Topics in Power Electronics*, vol. 3, no. 1, pp. 147–162, March 2015.

[42] *TMS320F2837xD Dual-Core Delfino Microcontrollers Technical Reference Manual*, Texas Instruments, January 2019, revised Version.

[43] *SN74LVC1G74 Single Positive-Edge-Triggered D-Type Flip-Flop with Clear and Preset*, Texas Instruments, January 2015, revised Version.